



Machine learning-driven classification of Pb—Zn ore deposits using pyrite trace elements and isotopic signatures: A case study of the Gunga deposit

Muhammad Amar Gul^{a,b}, Huishan Zhang^{c,*}, Yanguang Li^{c,*}, Xiaoyong Yang^{a,b}, Chao Sun^c, Xiaoqian Zhao^c, Guangli Ren^c, Asia Kanwal^d, Muhammad Hafeez^{a,b}, Yu Yang^{a,b}, Rizwan Sarwar Awan^e, Mohamed Faisal^{f,g}

^a CAS Key Laboratory of Crust-Mantle Materials and Environments, University of Science and Technology of China, Hefei 230026, China

^b CAS Center for Excellence in Comparative Planetology, University of Science and Technology of China, Hefei 230026, China

^c MNR Key Laboratory for the Study of Focused Magmatism and Giant Ore Deposits, Xi'an Center of Geological Survey, CGS, Xi'an 710054, China

^d Department of Mathematics, Kanazawa University, Japan

^e Northeast Petroleum University, Daqing, China

^f Department of Geology, Faculty of Science, Suez Canal University, El-Ismailia 41522, Egypt

^g School of Geosciences and Info-Physics, Central South University, Changsha 410083, China

ARTICLE INFO

Keywords:

Pyrite geochemistry
Machine learning algorithms
Metallogenic discrimination
leave-one-group-out cross-validation
Gunga deposit
CD-type deposits

ABSTRACT

The mineral pyrite, commonly associated with Pb—Zn deposits, can contain a variety of trace elements and is influenced by factors such as temperature, fluid composition, and metal source. These trace elements have long been used to differentiate between various types of Pb—Zn deposits. However, traditional discriminant diagrams, which typically rely on two or three dimensions, fail to comprehensively capture the complex relationships between pyrite trace elements and deposit types. To address this limitation, this study employed four machine learning algorithms—random forest (RF), support vector machine (SVM), gradient boost (GB), and multilayer perceptron (MLP)—to develop classification models based on pyrite trace element compositions. The models were trained on a dataset of 5400 data points from 134 mineral deposits or stratigraphic units with trace element data from published sources. The performance of the classifiers was evaluated via cross-validation using a variant of the leave-one-group-out (LOGO) method. The study applied these machine learning models to newly obtained geochemical data from pyrite samples collected at the Gunga Pb—Zn deposit in the Lasbela-Khuzdar metallogenic belt. The results demonstrated that the classifiers could accurately identify the source of Pb—Zn deposits, producing reliable predictive outcomes. Specifically, the models indicated that the geochemical signature of pyrite from the Gunga deposit was derived from sedimentary-hydrothermal fluids enriched in Pb, Zn, Sb, Tl, As, and Ge, which is consistent with geological and geochemical evidence. The in-situ $\delta^{34}\text{S}$ values of pyrite ranged from -24‰ to $+25\text{‰}$, suggesting that the sulfur in the deposit originated primarily from coeval seawater sulfate. Additionally, Pb isotope compositions indicated crustal sources for Pb—Zn in the Gunga deposit. The combined predictions from the classifiers, along with isotopic analyses of sulfur and lead, suggest that the Gunga Pb—Zn deposit is a Clastic-Dominant (CD)-type deposit. These findings highlight the effectiveness of machine learning techniques in classifying ore deposits and provide new insights into the origin of the Gunga Pb—Zn deposit.

1. Introduction

Accurate categorization of ore deposits at the beginning of an exploration project can significantly improve exploration efficiency by enabling the early use of predictive geological models. This enhancement is crucial when investigating beneath cover because of the elevated

expenses associated with drilling deep boreholes and when surface geology or geochemistry does not provide sufficient information about the deposit at depth (Dmitrijeva et al., 2020; Gregory et al., 2019; J. Zhang et al., 2022). Laser ablation inductively coupled plasma mass spectrometry (LA-ICP-MS) was used to analyze the trace element composition of particular minerals. These data are valuable because various ore

* Corresponding authors.

E-mail addresses: zhanghuishan.2086@163.com (H. Zhang), liyanguangok@126.com (Y. Li).

deposit types exhibit distinct fluid sources, metal sources, and depositional processes, all of which can significantly affect the trace element composition of the minerals formed. Moreover, these trace elements can remain intact inside mineral hosts during consecutive hydrothermal and metamorphic events. This study focused on pyrite because of its presence in various ore deposits, preservation of its trace element content up to mid-greenschist facies, and availability of extensive datasets containing the trace element contents of pyrite formed in sedimentary environments without hydrothermal influence (Frenzel et al., 2022; Xing et al., 2023; W.D. Zhang et al., 2022).

Conventionally, the cobalt-to-nickel ratio is one of the methods commonly employed to classify the nature of ore-forming fluids. However, two-dimensional discriminating plots, which are commonly used, have limitations compared with multidimensional information. Moreover, pyrite from different geological environments may exhibit similar compositions (Qin et al., 2024; Zhong et al., 2021). Machine learning (ML) presents novel approaches for analyzing pyrite geochemical data that differ from traditional methods. Recent studies have demonstrated that hydrothermal minerals, including pyrite, quartz, sphalerite, and apatite, can be accurately categorized based on trace element

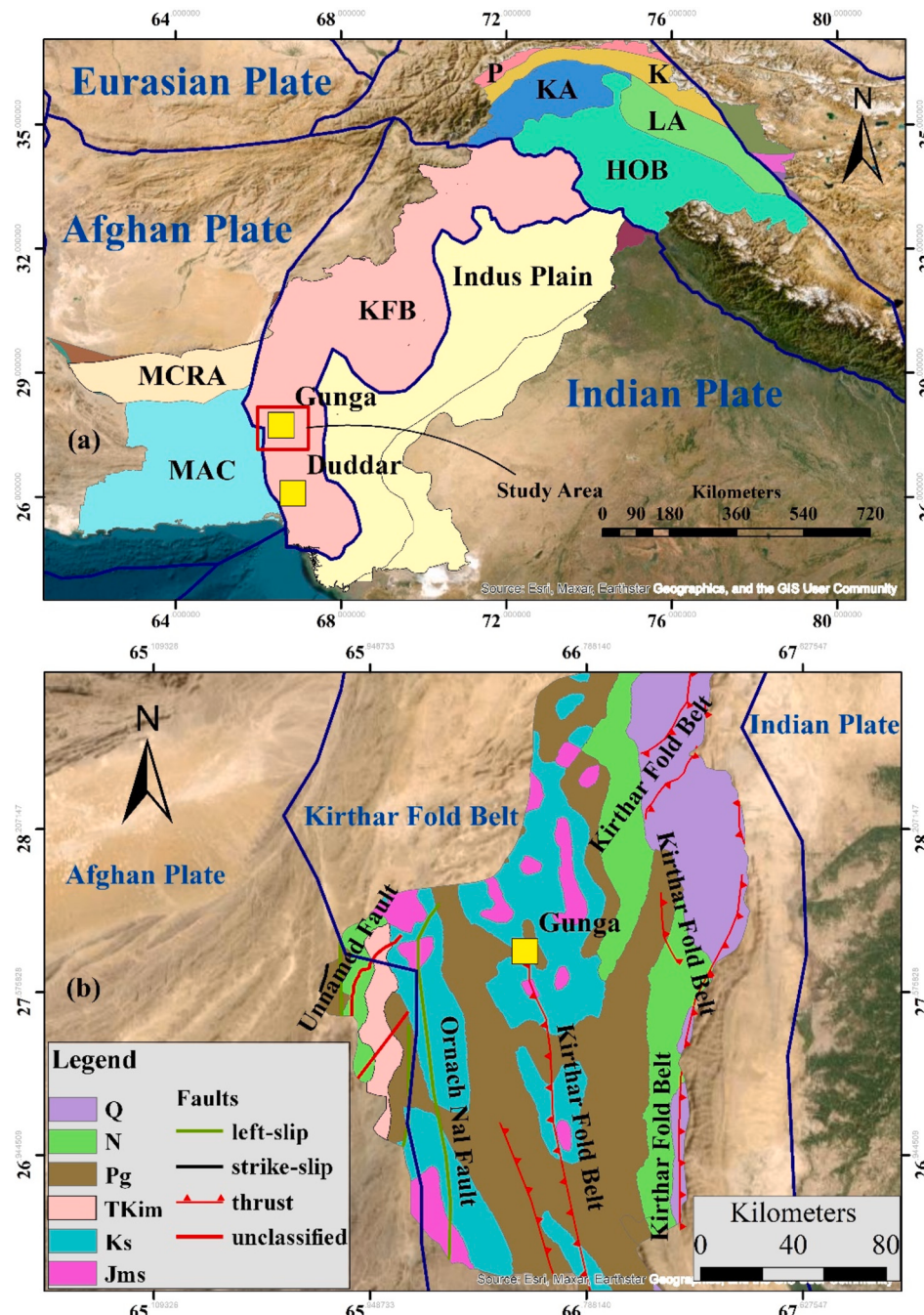


Fig. 1. (A) Geological Provinces of Pakistan and locations of Pb—Zn deposits. Data for the geological provinces were obtained from Hasterok et al. (2022). FTB: Fold and Thrust Belt, HOB: Himalayan Orogenic Belt, K: Karakoram, KA: Kohistan Arc, LA: Ladakh Arc, MAC: Makran Accretionary Complex, MCRA: Makran-Chaghai-Raskoh Arc, P: Pamir, Q: Qiantang. (B). Geology of District Khuzdar. Jms: Jurassic metamorphic and sedimentary rocks; Ks: Cretaceous Sedimentary rocks; TKim: Cretaceous and Tertiary igneous and metamorphic rocks; Pg: Paleogene sedimentary rocks; N: Neogene Sedimentary rocks; Q: Quaternary Sedimentary rocks. The bold blue line indicates Tectonic Plate boundaries. (For interpretation of the references to color in this figure legend, the reader is referred to the web version of this article.)

information and ML classification techniques. However, whether data-driven predictions align with geological evidence requires further investigation and application of the model. The objective of a machine learning classification model is to utilize historical data or existing knowledge to predict the categories of fresh data. A significant barrier to the advancement and enhancement of machine learning in the field of geology is the insufficient number of applications (Cui et al., 2023; X.M. Li et al., 2023; Sun et al., 2022; Williams et al., 2019; Zhong et al., 2021).

Situated along the western edge of the Indian Plate, the Gunga deposit (6.86mt; 11.4 % Zn and 2.1 % Pb) is a component of the Lasbela-Khuzdar metallogenic province (Fig. 1). The Early to Middle Jurassic Anjira Formation of the Ferozabad Group contains Pb—Zn mineralization (Jancovic, 1986; S.Nayar Ahsan, 1997). Jancovic (1986) discovered this deposit and described its geology, stratigraphy, and mineralogy. Husain et al. (2002) discussed the genesis of barite deposits using S isotope composition and trace elements, but no study has yet discussed the detailed ore genesis for Pb—Zn mineralization. The metallogenic belt for Pb—Zn mineralization is extensive, and at least one-third of it remains to be explored. Therefore, it is crucial to enhance our understanding of the mineralogy, temperature, and other physical and chemical factors governing ore mineralization to guide the exploration of new prospects and better comprehend known ones.

Previous studies on pyrite geochemistry using machine learning have not discriminated SEDEX-type pyrite from sedimentary pyrite, as suggested by Gregory et al. (2019), which is particularly useful for understanding ore genesis in sediment-hosted deposits. While earlier research focused primarily on gold deposits, this study, for the first time, utilized a large dataset of over 5400 geochemical data points, including SEDEX-type deposits, applied to sediment-hosted deposits. The leave-one-group-out (LOGO) approach was applied to 134 deposits treated as unseen data, offering practical insights for mineral exploration. A key issue addressed in this research is that LA-ICP-MS data points, often derived from the same specimen or pyrite grain, can lead to an overestimation of the classifier performance when both the training and testing sets include similar data. To avoid this, the study employed a cross-validation technique in which the dataset was divided into 134 subsets, each representing all samples from a single deposit, with classifiers trained on 133 deposits and tested on the remaining one. This process, repeated 134 times, ensured that the model performance was evaluated using completely unseen data, thereby providing a more accurate assessment of the classifiers' effectiveness in real-world applications.

We used LA-ICP-MS analyses of pyrite from various deposit types to train machine-learning algorithms to predict deposit types based on pyrite geochemistry. We created many categorization models using four distinct supervised machine-learning algorithms and evaluated them against conventional techniques, choosing the most effective ones for implementation. This study introduces novel LA-ICP-MS trace-element data for pyrite from the Gunga deposit. Utilizing these new data, we anticipate that machine learning-based data-driven techniques can be used to forecast the origin of ore-forming fluids and enhance our understanding of the genesis of Pb—Zn mineralization in the Gunga deposit. We provide a model that can differentiate deposit types and deduce the origin of Pb—Zn deposits by analyzing pyrite geochemical data and applying machine learning. The in-situ S—Pb isotope compositions of pyrite from the Gunga deposit were used to validate the predictions of the ML models. This tool also benefits the paleoceanographic community by addressing uncertainties regarding the existence or absence of hydrothermal influences, which can undermine trust in the reconstruction of past ocean conditions.

2. Regional geology

The geological context of the Lasbela and Khuzdar districts is connected to two significant tectonic events. The first event, which took place during the Late Triassic-Jurassic period, was the breakup of the

supercontinent Gondwana. At that time, the dominant processes were rifting and extensional tectonics, and sedimentation occurred in these settings. The vertical facies transition in the Jurassic Ferozabad Group, which was deposited in a transgressive continental shelf environment from land to the southeast, indicates a rifting process. The Ferozabad Group comprises clastic, platform shelf, and slope carbonate environments that progressed to distal quiescent conditions in the Early Cretaceous (Fig. 2) (Husain et al., 2002). The second orogenic event caused the separation of the Indo-Pakistan plate from the Turan block. The Indo-Pakistan plate collided with the Afghan and Central Iran-Lut blocks of the Eurasian plate in the west, resulting in the development of a fold belt and the obduction of the Bela-Khuzdar, Muslimbagh, Zhob, Waziristan, and Khost Ophiolitic complexes during the Late Cretaceous-Early Tertiary period (S.Nayar Ahsan, 1997; Zaigham and Mallick, 2000; Husain et al., 2002).

The Early-Middle Jurassic limestone, mudstone, shale, claystone, siltstone, and sandstone of the Ferozabad Group contain mineralization. Pre-Himalayan deformation is responsible for the tight and steeply descending isoclinal folds that define intensive folding. The Spingwar, Loralai, and Anjira are the three units that make up the Ferozabad Group. Although the Early Cretaceous Sember Formation lies at the top of the Ferozabad Group and is highly folded and disconformable in the Lasbela area, it is either completely missing or is only partially visible near Khuzdar. The Anjira Formation of interbedded Jurassic limestone and shale of the Ferozabad Group are linked to the Gunga deposit (Fig. 3) (S.Nayar Ahsan, 1997; Song et al., 2019).

The Geological Survey of Pakistan (GSP) uncovered primary lead-zinc and barite reserves in the Lasbela-Khuzdar Districts of Baluchistan, Pakistan. Specifically, the three most significant reserves in the area are Duddar in Lasbela (Zhang et al., 2024), Gunga/Surmai and Sekran in the Khuzdar district. Additionally, there are roughly 30 other prospects/occurrences, including Malkhor, Ranj Laki, and Mithi Nai in the Khuzdar district, and Kanrach and Dham Jal in the Lasbela district. Zinc, lead, and barite are frequently discovered in carbonate rocks as veins and replacement deposits, as well as in strata-bound deposits associated with black shales, mudstones, argillaceous limestones, and pyroclastic brecciated rocks (Gul et al., 2020). These deposits are thought to be either exhalative sedimentary or Mississippi valley type. According to an estimate, with a combined grade of 14–16 % Zn—Pb, proven deposits range over 16mt (Jancovic, 1986; S.Nayar Ahsan, 1997). However, the various types of mineralization are not yet fully understood.

3. Gunga deposit geology

The mineralized unit, extending over an area of 1500–2000 m in length and 600–1000 m in width, has a thickness of 100–200 m (Fig. 4). It comprises multiple distinguishable members: barren limestone and shale bed, lower mineralization unit (LMZ), barren limestone and shale bed, upper mineralization zone (UMZ), and siliceous sinter above, starting from the bottom and progressing upward (Fig. 4) (Jancovic, 1986). The descriptions of these units are as follows.

The footwall is composed of interbedded carbonaceous shale and siltstone, with a gradual transition to mineralized siltstone and shale. This transition is marked by occasional patches of pyrite/marcasite and ore minerals such as galena and sphalerite found in the uppermost portion of the footwall rocks. The **lower mineralized zone** is closely linked to a series of hydrothermal and hydrothermally altered sediments, including siliceous sinter, siltstone, and siderite. The lower Pb—Zn mineralized zone has lenses and irregular veins formed along the brecciated zone. Mineralization is dominantly stratiform relative to the enclosing rocks, but in places, it is epigenetic as fracture/open space fillings (Figs. 3 and 5). The mineralized bodies mostly contain over 6 % Zn and 1.5 % Pb, and some places exceed 10 %.

Above the lower mineralized zone lies a **barren bed** of interbedded black, dark-grey bituminous fossiliferous argillaceous limestone and

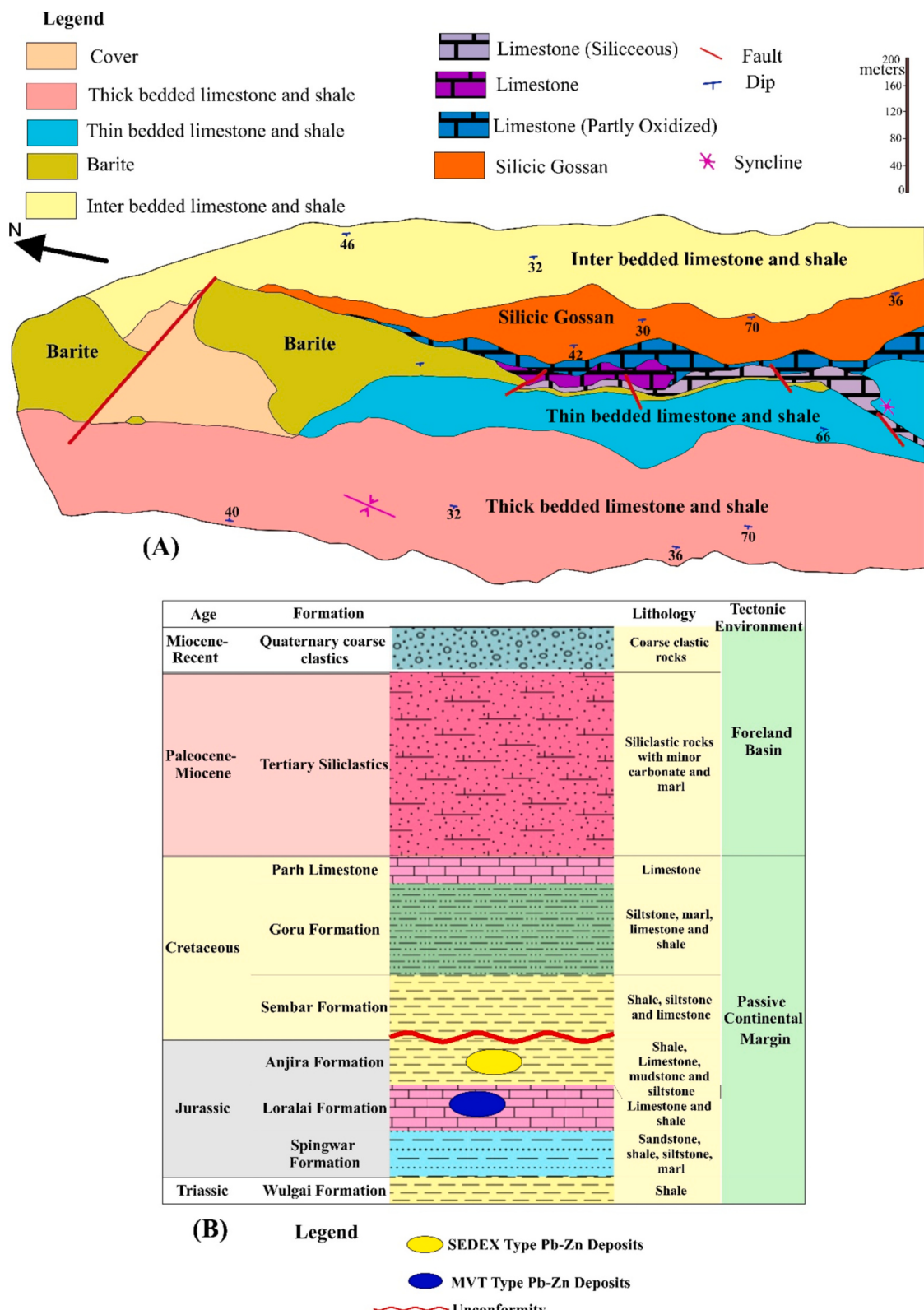


Fig. 2. (A) Geological map of the Gunga Mine, District Khuzdar (B). Stratigraphic column of the Lasbela-Khuzdar region (S.Nayar Ahsan, 1997).

shale with some siltstone. This bed contains disseminated tiny frambooidal and spheroidal pyrite, which are likely syngenetic and associated with bacterial activity, although they are generally devoid of mineralization. The thickness of this bed ranges from 50–100 m.

The **upper mineralized zone** is situated above the barren limestone and shale bed. The footwall is a bed of siliceous sinter mixed with

brownish argillaceous material, and dark-brown disseminated bituminous matter is frequently found in argillite. The upper mineralized zone is characterized by an increasing presence of disseminated barite, Fe—Zn, and Pb sulfides. This zone transitions into a transition zone with a thickness of a few meters, which leads to the main mineralization of galena, sphalerite, and marcasite/pyrite. The main mineralization was

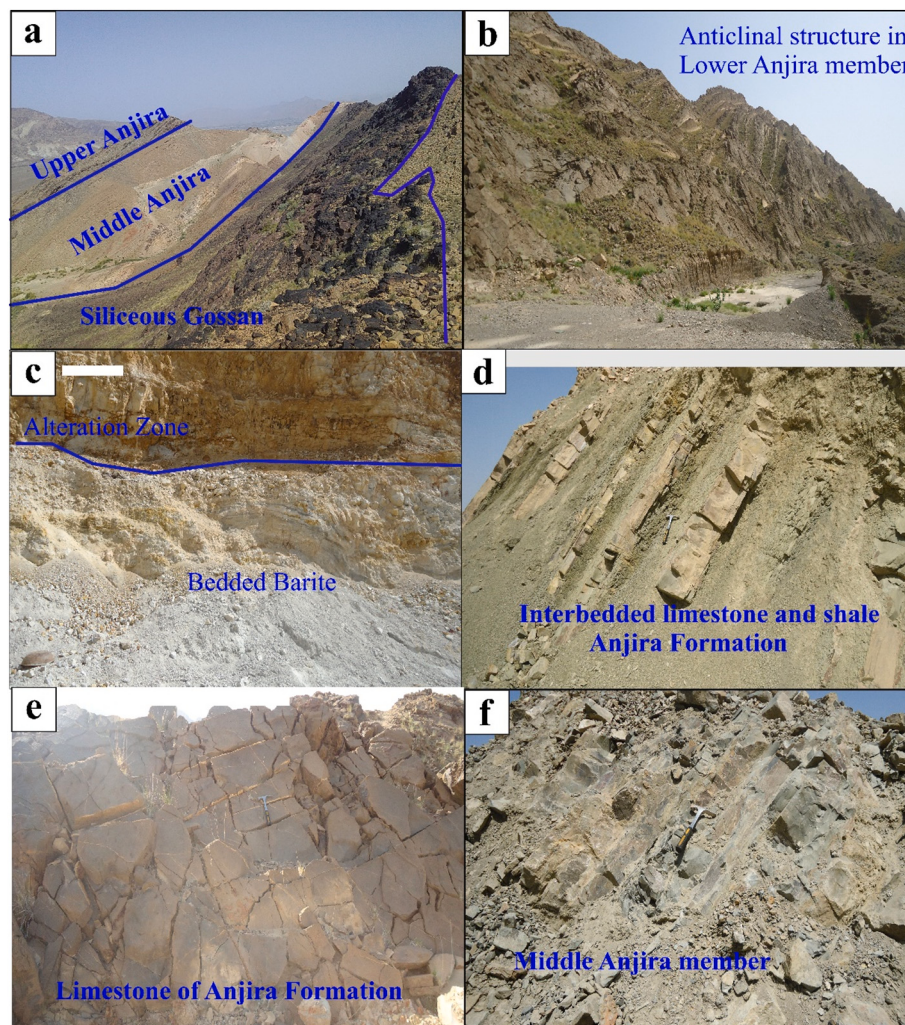


Fig. 3. Field photographs of different facies of the Anjira Formation (host rock) in the Gunga region, District Khuzdar, showing folded structures, bedded facies, contacts between different facies, mineralized gossan, layered barite, and alteration zones.

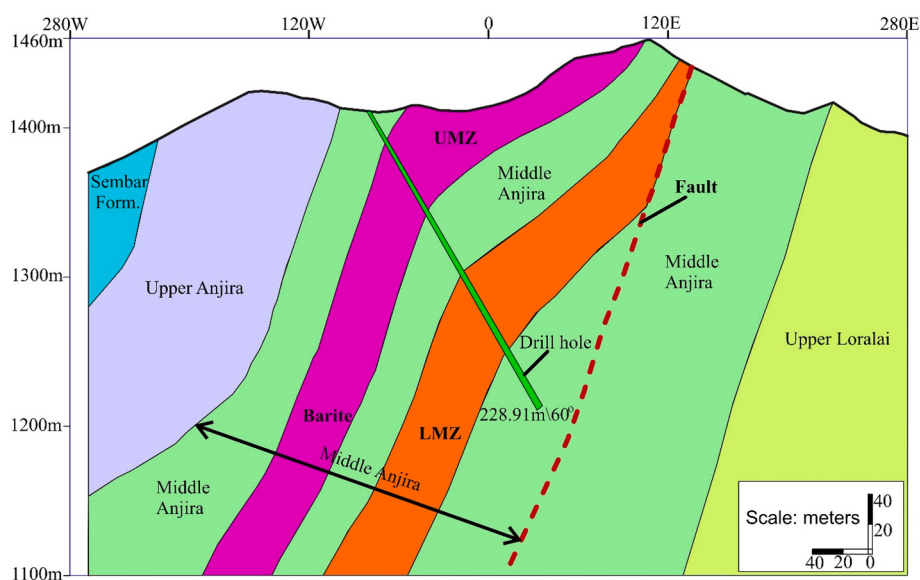


Fig. 4. Map of the subsurface structure of the Gunga deposit showing different mineralized zones and the location of the drill hole. It is clear from the map that mineralization occurred in the middle part of Anjira. LMZ = lower mineralization zone, UMZ = upper mineralization zone.

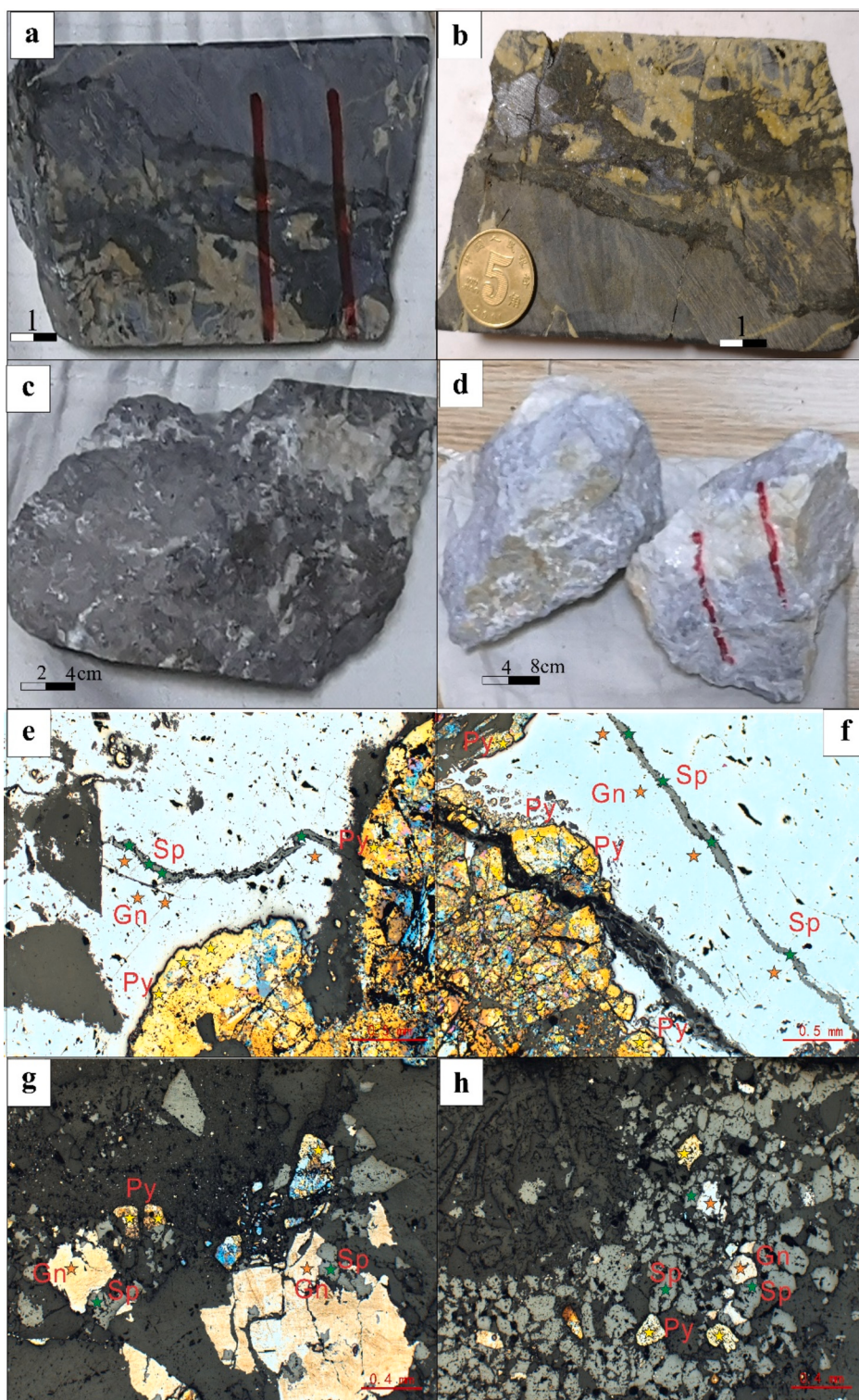


Fig. 5. Photograph clearly showing different minerals from the Gunga Pb—Zn deposit: (a-b) Core samples containing ore minerals such as Sphalerite, Pyrite, and Galena. (c) Outcrop sample with ore minerals. (d) Barite sample from UMZ. (e-f) Microphotographs showing ore minerals and vein structure of Sphalerite from LMZ. (g-h) Disseminated Sphalerite and other ore minerals from the UMZ. Sp: Sphalerite, Gn: Galena, Py: Pyrite.

associated with the barite bed in the central part of the upper mineralized zone. The ore minerals in the lower portion of the barite-bearing zone existed as lenses, patches, and streaks, and there was no sharp transition in the zones containing variable amounts of ore minerals (Figs. 3 and 5). The hanging wall of the mineralized bed was marked by barite mineralization with traces of galena, marcasite, and occasional sphalerite. The uppermost mineralized unit consists of a bed of siliceous

sinter, which can be several meters thick, with an abundance of impurities, such as limestone and argillite, as well as local barite grains (Jancovic, 1986; S.Nayar Ahsan, 1997).

The mineral associations in the LMZ and UMZ exhibited similar mineralogical features, with the primary difference being in the concentrations of individual minerals. Mineral paragenesis, which includes sphalerite, galena, and pyrite as the main ore minerals, is accompanied

by traces of chalcopyrite and cinnabar. In the oxidation zone, jarosite, geothite, smithsonite, cerussite, and iron oxides were dominant, and traces of native sulfur were also present. The major element contents of the ore minerals are presented in Table 2, and complete mineral paragenesis is illustrated in Fig. 6. Sphalerite was the dominant mineral, while galena was the subordinate ore mineral (Fig. 5). Sphalerite was found as vein-like structures in the LMZ and as disseminated mineralization in the UMZ. In contrast, pyrite was found as large crystals and was less hydrothermally altered in the LMZ, whereas in the UMZ, pyrite crystals were small and hydrothermally recrystallized, as indicated by their chemical composition. Fractured galena was observed in the LMZ and disseminated in the UMZ.

4. Sampling and analytical methods

4.1. Field and experimental work

During three field excursions conducted from 2018 to 2020, a comprehensive collection of 120 representative samples was obtained from the host rocks, mineralized zones, and alteration areas of the sulfide deposits under study. In addition, five drill core samples were obtained from drill holes located within the research area. The selection of sample locations relied heavily on the presence of exposed rock formations. The samples were large, uniform, and minimally affected by weathering. They were collected meticulously, considering the variations in color, texture, and macroscale mineralogy. The samples were cut and polished to obtain thin sections for microscopic examination. The chosen samples were obtained from both surface and underground mines, and their sulfide mineralogy, textural characteristics, and paragenetic sequences were analyzed. Transmission and reflected light microscopy were used for the analysis. Furthermore, representative samples were selected from both zones for in situ S and Pb isotope studies, as well as for further analysis using LA-ICP-MS and EPMA to identify major, minor, and trace elements.

These studies were conducted at the State Key Laboratory of Continental Dynamics, Northwest University, Xi'an, China (in situ S—Pb isotope analysis) and the Xi'an Center of Geological Survey, CGS (EPMA), Xi'an Zhaonian Mineral Testing Technology Co., Ltd., Xi'an, China (LA-ICP-MS). Supplementary Document 1 contains the specifics of the analytical techniques.

4.2. Machine learning algorithms

4.2.1. Data collection

The dataset on trace elements in pyrite was compiled from 134 sites and over 5400 LA-ICP-MS data points sourced from peer-reviewed papers and doctoral theses (Cameron, 2011; Gregory et al., 2019; Mukherjee et al., 2019). The dataset includes several types of pyrite deposits: metamorphic ($n > 1800$), magmatic ($n > 900$), barren sedimentary ($n = 1900$), and mineralized pyrite (CD, $n > 700$). The details are provided in Supplementary Table S1. Each examined point in the sample data set was recorded with characteristics such as Co, Ni, Cu, Zn, As, Se, Ag, Sb, Pb, Bi, and Tl. Sedimentary pyrite found in shales reflects changes in seawater chemistry, whereas CD pyrite from basinal brines or hydrothermal fluids contains commercial metals such as Pb, Zn, Cu, Cd, and Ge (Gregory et al., 2019). The pyrite samples in the dataset were crucial because they specifically reflected the major mineralization stage without being affected by pre-metallogenic and post-metallogenic influences when used in the classifier. Data from the Gunga deposit were omitted to avoid data leakage and prevent artificial inflation of the forecast accuracy. Pyrite samples with inclusions were not omitted because of the significance of their characteristics.

4.2.2. Data processing

Data processing plays a crucial role in converting raw data into suitable and comprehensible formats to ensure optimal performance and accurate outcomes. A set of procedures is required to address the issue of missing values (Alferez et al., 2022; Han et al., 2019; He et al., 2022; Qin

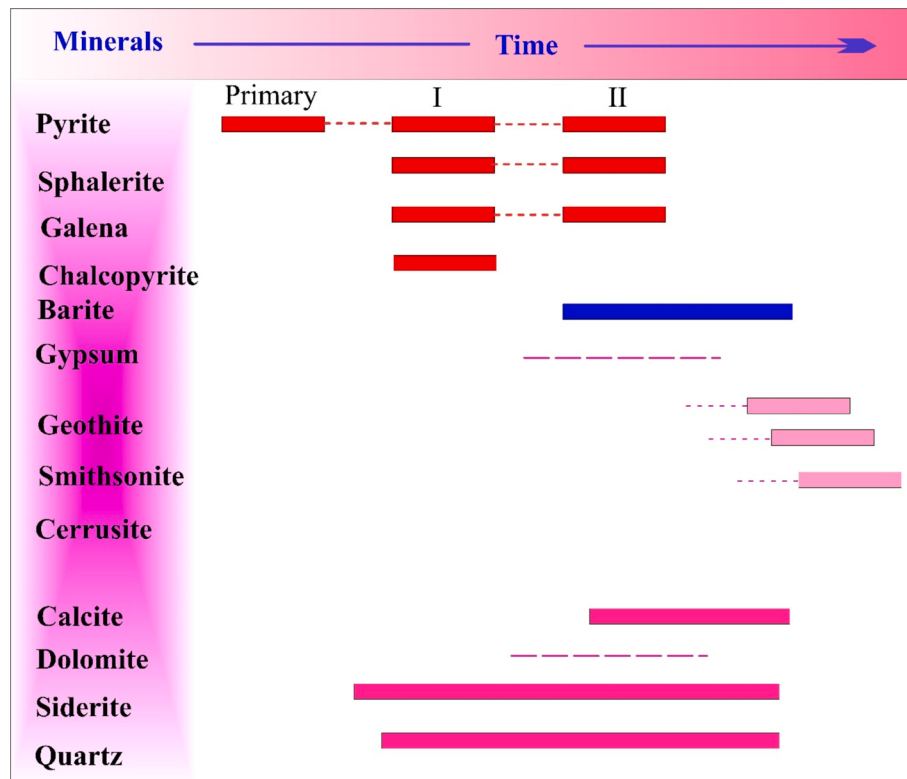


Fig. 6. Ore paragenesis of the Gunga deposit showing different mineral presence from the early to late stages of mineralization.

et al., 2024; Sun et al., 2022; Zhong et al., 2021). In many cases, missing values are replaced by detection limits (DL). LA-ICP-MS studies with the highest number of missing values were excluded from the Feature Selection process. The trace element data underwent log transformation to address a broad range of data from various aspects. Subsequently, normalization was performed using the conventional scaler approach with the Z-score method. To prevent unpredictable mistakes, the dataset was randomized before each trial.

4.2.3. Feature selection and data splitting

Various datasets may possess disparate elements stemming from variations in the research objectives. Consequently, some of the samples had missing values. It is crucial to evaluate the optimal balance between the number of samples and features. We have employed feature importance analysis using both RF and GB models, focusing on elements such as Co, Ni, Cu, Zn, As, Se, Ag, Sb, Pb, and Bi. These elements have also been identified in previous studies. Our results reveal that Se and Pb possess the highest importance, while Co exhibits the lowest importance value in both the GB and RF models (as depicted in Fig. 7).

The dataset for trace element pyrite was partitioned into two groups for model use: training and testing sets. The training set was employed to train the machine learning algorithms, whereas the testing set was used to evaluate the performance of the model. To ensure an accurate evaluation of model performance, the testing set was concealed from the

model during the training process. According to Qin et al. (2024), resampling strategies do not consistently improve the performance of machine learning models, except for the multilayer perceptron (MLP). Other machine learning models may be less affected by class imbalance owing to their capacity to process multidimensional data with sparse features.

4.2.4. Machine learning algorithms

Identifying the origin of pyrite is a common classification task, and numerous supervised machine learning methods have demonstrated effectiveness in making class predictions based on multiple input variables (Qin et al., 2024; Sun et al., 2022; Zhong et al., 2021). For multiclass classification tasks, four effective supervised machine learning techniques were employed: RF, SVM, GB, and MLP. A comprehensive explanation of these algorithms is provided in Supplementary Document 1. Our objective was to enable each model to exhibit outstanding classification performance. Typically, every method requires the selection and adjustment of one or more parameters to achieve optimal model performance.

Grid search and cross-validation techniques were employed to determine the optimal hyperparameters for the fine-tuning algorithms. Table 1 provides a comprehensive list of the machine learning algorithms utilized, along with their respective parameter settings. Four classification algorithms were assessed to determine the most effective and subsequently employed to construct classifiers for predicting new data from the Gunga deposit. To ensure the reliability and accuracy of our predictive models, it is essential to conduct a thorough evaluation of their predictions. The performance of the algorithms was assessed using metrics such as accuracy, area under the curve (AUC), and LOGO (Qin et al., 2024; Sun et al., 2022; Zhong et al., 2021).

5. Results

5.1. Microscopic investigations

Petrographic analysis reveals that pyrite from the lower mineralization zone (Pyrite-I) is characterized by inclusion-free, large anhedral crystals with irregular morphology, ranging from 40 to 265 µm in diameter (Fig. 5e-f). These crystals show primary intergrowth with chalcopyrite, while smaller grains commonly occur within sulfide-bearing fractures. Local replacement textures by chalcopyrite and sphalerite are observed along crystal boundaries. In situ mineral analysis indicates homogeneous chemical composition within individual grains, as discussed in detail in the following sections.

In the upper mineralization zone, Pyrite-II occurs as fine-grained crystals (35–80 µm width, 60–195 µm length), exhibiting subhedral to euhedral shapes, with a tendency toward cubic forms (Fig. 5g-h). These crystals commonly form overgrowths around larger chalcopyrite grains and show a predominant association with sphalerite. Characteristic features include galena inclusions, brecciated textures, and framboidal structures. Notably, these crystals lack compositional zoning.

5.2. Major elements concentration in pyrite

The lower mineralization zone had a higher pyrite concentration than the upper mineralization zone in the Gunga deposit. In the Gunga

Table 1
Machine learning algorithms and their important parameters.

Methods	Parameters
RF	max_depth = 20, n_estimators = 400
MLP	activation = tanh, alpha = 0.0001, hidden_layer_sizes = (50, 100, 50), learning_rate = constant, solver = adam
SVM	C = 100, gamma = 0.1, kernel = rbf
GB	learning_rate = 0.1, max_depth = 5, n_estimators = 300

Fig. 7. Importance of different trace elements (as a feature) present in pyrite measured using machine learning algorithms (RF and GB).

deposit, the lower mineralized zone (pyrite-I) has varying levels of minor and trace element contents compared to the upper mineralized zone (pyrite-II) with 51.9 wt% S and 45.7 wt% Fe in pyrite-I while 52.5 wt% S and 45.64 wt% Fe in pyrite-II, which are less than their standard values present in pyrite, as shown in Fig. 8 and Table 2. S and Fe ratios

>2 indicate Fe loss, whereas ratios <2 indicate S loss. The S/Fe-calculated pyrite content in the Gunga deposit was mostly less than two, except at three points.

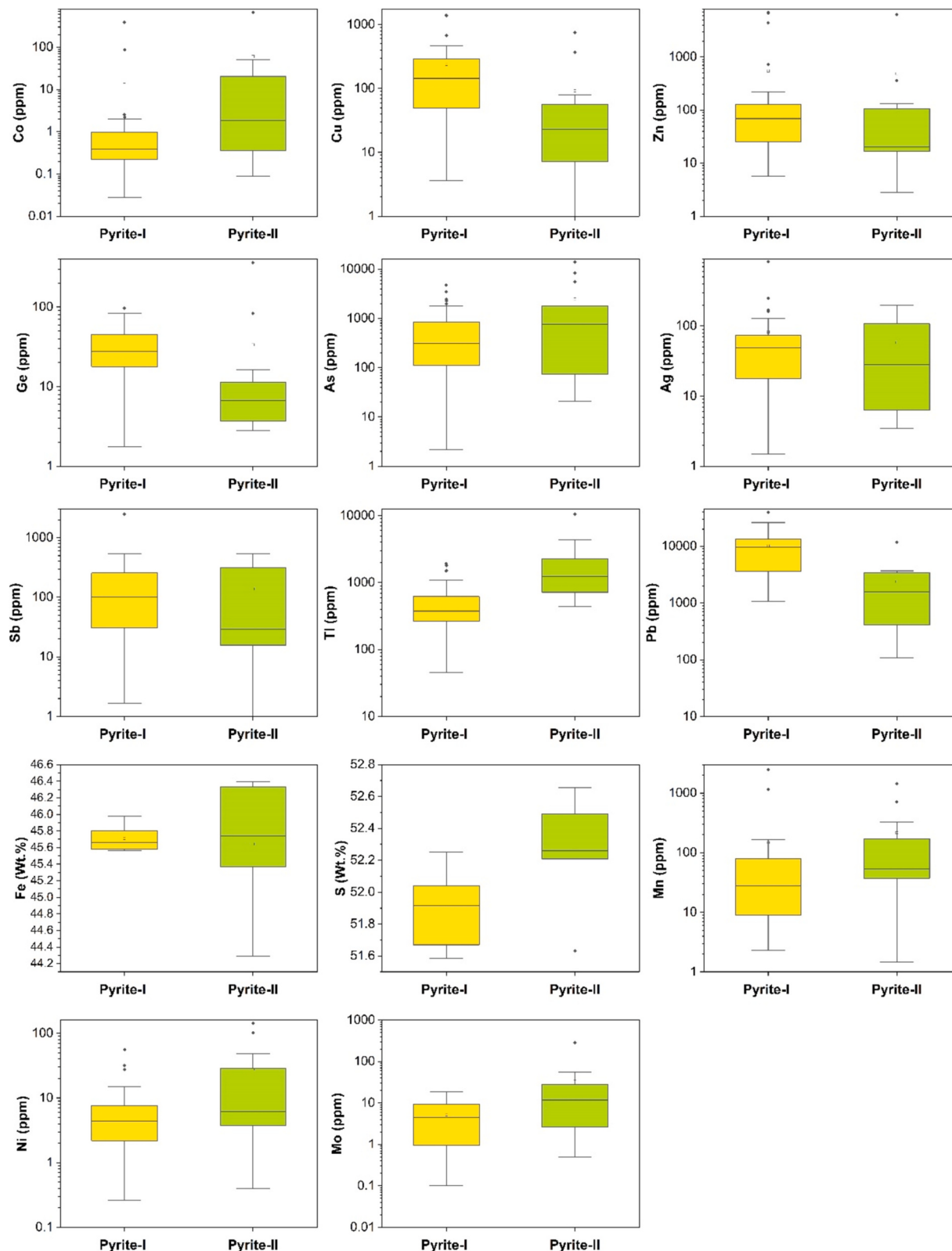


Fig. 8. Box plots of major, minor, and trace elements in Pyrite of both Upper and Lower mineralization zones from the Gunga Pb—Zn deposit.

Table 2

Major element concentrations (wt%) in Pyrite from the Gunga Deposit. (bdl: below detection limit).

S no.	Zn	Fe	Pb	S	Cd	Mo	Ga	Cu	Total
1	0.05	44.29	1.21	51.63	bdl	0.73	0.10	0.04	98.04
2	0.03	45.37	0.19	52.49	0.04	2.48	0.07	0.03	100.70
3	63.12	2.42	0.08	32.35	0.03	0.49	0.05	bdl	98.54
4	0.05	46.39	0.00	52.21	bdl	0.68	0.10	bdl	99.43
5	0.03	46.33	0.04	52.29	0.01	2.59	0.07	bdl	101.37
6	0.25	45.88	0.06	52.65	bdl	0.70	bdl	bdl	99.55
7	0.06	45.61	0.22	52.23	0.00	0.76	0.13	0.01	99.02
8	bdl	45.80	0.95	52.04	bdl	0.63	0.03	0.02	99.47
9	bdl	45.98	0.58	52.25	0.01	2.52	0.16	0.05	101.55
10	0.02	45.56	1.51	51.67	bdl	0.67	0.08	bdl	99.50
11	bdl	45.74	0.58	51.89	0.02	0.67	0.15	0.07	99.12
12	bdl	45.59	0.96	51.94	bdl	0.78	0.07	0.03	99.37
13	0.10	45.58	0.45	51.58	0.00	0.69	0.05	0.00	98.47
14	0.05	46.39	bdl	52.21	bdl	0.68	0.10	bdl	99.43
15	0.03	46.33	0.04	52.29	0.01	2.59	0.07	bdl	101.37
16	0.25	45.88	0.06	52.65	bdl	0.70	bdl	bdl	99.55
17	0.06	45.61	0.22	52.23	0.00	0.76	0.13	0.01	99.02
18	bdl	45.80	0.95	52.04	bdl	0.63	0.03	0.02	99.47
19	0.02	45.56	1.51	51.67	bdl	0.67	0.08	bdl	99.50
20	bdl	45.74	0.58	51.89	0.02	0.67	0.15	0.07	99.12

5.3. Minor and trace elements

LA-ICP-MS studies were conducted on representative samples from the Gunga deposit, with 39 data points from Pyrite-I and 21 from Pyrite-II (Table 3). This study assembled the findings of the statistical analysis of pyrite trace elements and used a box-and-whisker plot to illustrate the data variation among the different types of deposits (Fig. 9). Some outliers may indicate a high concentration of elements in the pyrite structure, whereas others may be due to foreign materials trapped inside the pyrite. Recent studies have shown significant connections between inclusions found in minerals and different types of ore deposits, providing assurance for investigating the data stored in pyrite inclusions (Dmitrijeva et al., 2020; Gregory, 2014; Qin et al., 2024; Sun and Zhou, 2022; Zhong et al., 2021). Thus, these elevated values were retained as relevant data and were not treated as interference. Fig. 9 illustrates how an element contributes to the partial distinction between various forms of pyrite. The average and intermediate values of the components, including Cu, Zn, As, Se, Pb, and Ag, in the CD deposits were greater than those in the barren sedimentary pyrite. The minor and trace element contents in pyrite from the Gunga deposit were as follows:

The concentrations of several elements in the pyrite samples from the Gunga deposit were consistent with those typically found in the CD deposits. Zn concentrations ranged from 2 to 6908 ppm, with an average of 526 ppm, aligning with the values reported in previous studies. Cu concentrations, ranging from 2 to 1400 ppm with an average of 194 ppm, were also in line with the levels found in the CD pyrite. Similarly, Mn levels, ranging from 2 to 2472 ppm with an average of 168 ppm, were consistent with sedimentary pyrite, although higher than those in magmatic deposits (Fig. 8) (Cameron, 2011; Mukherjee and Large, 2017; Qiu et al., 2018).

In contrast, certain elements were found in higher concentrations in CD pyrite. Pb ranged from 109 to 39,814 ppm, with a mean value of 8210 ppm, which exceeded the levels observed in previous studies. Tl concentrations varied between 45 and 10,601 ppm, with an average of 1000 ppm, which is significantly higher than that previously reported for CD pyrite. The Ag concentrations, ranging from 2 to 820 ppm with an average of 76 ppm, and the Sb levels, ranging from 2 to 2465 ppm with an average of 188 ppm, were also higher than those typically found in CD deposits. Additionally, As concentrations, which ranged from 3 to 14,029 ppm with an average of 1209 ppm, were comparable to those in previous studies but still displayed some elevated values (Fig. 9) (Cameron, 2011; Mukherjee and Large, 2017.; Qiu et al., 2018).

On the other hand, several elements were found in lower concentrations than those typically observed in CD pyrite. The Mo

concentrations ranged from 2 to 287 ppm, with an average of 14 ppm, and the Ni levels ranged from 2 to 144 ppm, with an average of 14 ppm, both of which were below the typical concentrations reported for CD pyrite. Co, with concentrations ranging from 2 to 670 ppm and an average of 28 ppm, was also significantly lower than the levels commonly found in CD deposits (Figs. 8 and 9) (Cameron, 2011; Mukherjee and Large, 2017; Qiu et al., 2018).

5.4. S isotope compositions

Fig. 10 presents the in-situ isotope analysis results of pyrite from both zones of the Gunga deposit. The $\delta^{34}\text{S}_{\text{CDT}}$ values of pyrite-I varied from -15.05 to 20 ‰, with an average value of -0.18 ‰ ($n = 11$). On the other hand, the $\delta^{34}\text{S}_{\text{CDT}}$ values of pyrite-II ranged from -23.49 to 26 ‰ ($n = 09$) with an average value of 0.75 (Table 4).

5.5. Pb isotope compositions

The $^{206}\text{Pb}/^{204}\text{Pb}$ ratios of pyrite ($n = 16$) ranged from 18.54 to 18.56, the $^{207}\text{Pb}/^{204}\text{Pb}$ ratios ranged from 15.68 to 15.71, and the $^{208}\text{Pb}/^{204}\text{Pb}$ ratios ranged from 38.71 to 38.77 (Table 5). These values are plotted in the Pb isotope evolution diagram presented by Zartman and Doe (1981) in Fig. 11.

5.6. ML algorithms

Table 6 shows the results of various machine learning algorithms using processed and standardized data. Each model was replicated ten times using various random seeds to prevent potential bias in the predictions. The MLP and SVM models had the highest accuracy (> 91 %) and AUC (> 0.98) among the standardized data models, whereas RF and GB demonstrated strong performance. The results indicate that machine learning techniques, including MLP, GB, RF, and SVM, are effective and strong in distinguishing between various forms of pyrites (Fig. 12).

Supplementary Tables S2 and S3 present confusion matrices for the validation and test sets, respectively. These results demonstrate the classification accuracy of each group in the testing set. Overall, MLP, RF, and SVM exhibited strong predictive performance. Each model showed differing levels of effectiveness in predicting various types of pyrite. The MLP model had the highest accuracy in predicting CD and sedimentary pyrite, whereas the GB model performed the best in predicting magmatic pyrite.

Table 3

Minor and trace elements concentration (ppm) in Pyrite (bdl; below detection limit).

S no.	Mn	Co	Ni	Cu	Zn	Ge	As	Se	Mo	Ag	Sn	Sb	Hg	Tl	Pb
Pyrite-I															
1	27.84	0.88	4.05	1400.63	51.03	71.45	553.90	bdl	9.21	819.65	0.41	289.82	8.47	272.33	25,423.63
2	30.90	0.58	7.66	281.57	59.77	16.87	1225.63	0.67	6.26	70.88	0.37	170.71	0.32	487.52	7725.44
3	81.24	0.20	2.13	136.25	4361.27	33.44	194.87	0.09	1.24	48.84	1.57	64.78	0.86	469.16	11,246.46
4	78.50	0.30	2.79	229.25	66.13	19.23	412.17	0.21	2.16	74.35	0.20	94.75	0.81	618.46	11,084.60
5	92.06	0.27	1.18	180.81	6772.66	31.60	170.67	0.45	0.50	56.72	2.03	16.44	0.88	288.07	9618.06
6	34.98	0.12	6.06	292.43	103.01	26.35	2258.77	0.59	9.90	111.77	0.24	255.41	0.73	678.90	15,743.71
7	13.11	0.84	1.88	417.37	19.61	52.98	309.75	0.46	1.91	170.41	0.24	101.32	5.55	562.42	14,567.13
8	4.61	0.03	0.26	1384.16	23.08	30.46	8.84	1.78	0.18	250.24	0.24	7.23	1.18	1926.46	3613.58
9	5.73	86.58	27.55	672.61	217.72	27.50	900.41	bdl	13.06	251.21	0.48	2465.50	2.16	106.16	10,817.25
10	93.12	0.30	3.98	461.39	99.15	30.81	29.99	bdl	0.10	168.64	0.33	36.09	9.99	446.58	13,495.64
11	22.51	2.53	15.14	145.73	80.77	17.89	1967.15	0.36	9.21	62.76	0.18	254.52	0.59	468.24	11,621.09
12	20.67	0.42	1.55	100.35	33.74	96.88	796.47	0.30	9.24	58.57	0.30	209.56	2.68	275.23	26,155.94
13	68.68	0.98	12.78	370.07	51.16	17.58	125.95	0.47	0.47	63.83	0.21	90.34	1.94	646.28	11,437.65
14	47.13	0.09	4.75	129.41	68.77	21.62	1759.32	0.46	10.12	39.13	0.30	176.77	0.28	488.58	7199.13
15	bdl	2.52	1.73	44.28	102.33	26.94	188.15	0.40	2.23	21.65	0.58	371.37	0.27	87.29	9686.63
16	bdl	0.37	5.05	145.31	127.47	20.85	1790.19	0.42	10.06	73.63	0.52	233.79	0.48	255.68	10,377.14
17	bdl	0.65	7.12	249.38	135.35	20.57	136.21	0.21	0.66	70.62	0.19	59.70	1.17	258.62	13,773.21
18	bdl	2.00	10.06	70.21	181.71	13.66	3475.07	1.40	17.51	22.17	0.90	344.76	0.25	267.03	10,932.40
19	67.94	2.21	3.25	152.43	175.05	17.23	111.17	0.61	0.45	37.64	0.11	55.06	0.83	358.54	8663.85
20	128.31	0.22	2.30	134.64	78.48	17.96	685.27	0.08	4.53	38.69	0.16	180.07	bdl	342.36	13,082.53
21	2472.24	1.57	31.71	155.58	85.09	23.45	4769.51	bdl	18.38	25.58	0.10	437.80	bdl	313.45	6081.66
22	1149.62	1.90	11.79	370.70	6908.87	54.28	158.94	0.64	0.46	59.86	1.65	101.25	bdl	227.62	39,814.50
23	9.54	0.11	2.14	81.33	31.51	49.53	26.51	0.81	0.50	11.92	0.04	9.07	bdl	390.64	2394.30
24	11.23	0.24	5.13	39.46	17.35	38.18	628.92	bdl	4.83	14.00	0.16	541.74	bdl	167.20	4060.81
25	66.52	0.13	7.54	143.75	117.43	31.10	2464.58	0.95	11.79	50.89	0.29	160.80	1.41	373.31	7866.98
27	123.00	0.09	2.19	405.00	106.00	31.10	22.40	bdl	bdl	160.00	bdl	17.40	bdl	1092.00	13,404.00
28	2.89	0.06	4.37	42.80	9.49	47.60	43.30	bdl	1.32	15.70	bdl	30.50	bdl	591.00	2354.00
29	9.48	bdl	bdl	275.00	28.10	45.50	67.20	bdl	1.55	128.00	bdl	33.60	bdl	282.00	8939.00
30	15.30	0.31	bdl	85.60	77.00	83.00	606.00	bdl	4.90	21.30	bdl	134.00	bdl	327.00	20,550.00
31	165.00	0.72	10.50	359.00	220.00	17.00	137.00	bdl	0.42	83.80	bdl	73.50	bdl	828.00	12,244.00
32	3.24	bdl	bdl	3.59	10.90	70.30	2.17	bdl	bdl	1.50	bdl	1.67	bdl	182.00	3370.00
33	bdl	0.38	3.12	16.60	5.60	6.68	212.00	bdl	4.51	17.70	bdl	274.00	bdl	248.00	2079.00
34	bdl	bdl	bdl	14.00	6.96	23.90	777.00	bdl	2.03	4.69	bdl	16.80	bdl	277.00	3441.00
35	2.29	0.27	1.57	49.10	25.30	7.43	92.00	bdl	1.84	7.62	bdl	20.70	bdl	1810.00	1059.00
36	29.30	388.00	55.80	95.60	726.00	1.77	480.00	bdl	5.43	42.40	bdl	420.00	bdl	45.20	1950.00
37	7.18	bdl	bdl	37.20	25.30	16.10	27.60	bdl	bdl	8.27	bdl	16.40	bdl	1494.00	2748.00
38	3.66	bdl	bdl	50.80	27.00	31.90	757.00	bdl	5.54	17.50	bdl	108.00	bdl	1014.00	4264.00
39	5.58	0.63	5.61	38.40	35.90	59.90	851.00	bdl	9.40	23.10	bdl	139.00	bdl	450.00	16,654.00
40	8.91	bdl	bdl	2.27	13.60	16.90	36.20	bdl	4.36	4.69	bdl	29.30	bdl	1517.00	2192.00
Pyrite-II															
1	326.00	50.10	28.60	56.10	361.00	5.02	14,029.00	bdl	287.00	118.00	bdl	541.00	bdl	1952.00	2162.00
2	1.48	bdl	bdl	0.42	2.78	6.96	44.50	bdl	bdl	3.44	bdl	0.70	bdl	1162.00	410.00
3	60.60	bdl	bdl	15.30	16.60	8.74	137.00	bdl	11.70	20.10	bdl	31.40	bdl	998.00	3514.00
4	60.10	22.30	4.67	45.80	131.00	5.39	5562.00	bdl	25.30	68.50	bdl	330.00	bdl	1418.00	3442.00
5	37.40	0.09	bdl	23.00	17.10	4.03	73.50	bdl	2.04	25.80	bdl	18.20	bdl	511.00	892.00
6	172.00	0.28	bdl	6.09	17.80	2.81	1397.00	bdl	bdl	17.00	bdl	18.30	bdl	442.00	253.00
7	716.00	0.36	bdl	7.14	19.90	3.09	689.00	bdl	bdl	4.37	bdl	27.00	bdl	719.00	109.00
8	37.40	0.77	5.49	19.30	57.40	3.02	217.00	bdl	0.50	142.00	bdl	11.50	bdl	4345.00	186.00
9	57.70	4.17	14.00	37.90	76.70	3.41	1440.00	bdl	2.67	196.00	bdl	46.50	bdl	4204.00	1225.00
10	49.30	bdl	bdl	3.80	9.35	6.46	74.30	bdl	6.24	5.35	0.24	15.80	bdl	673.00	1773.00
11	31.90	bdl	bdl	2.71	8.51	10.80	20.70	bdl	1.47	6.31	bdl	39.20	bdl	1702.00	3674.00
12	37.56	20.61	6.92	74.59	32.11	11.98	8308.20	bdl	23.63	64.66	0.46	317.31	30.85	2263.97	11,832.15
13	bdl	0.10	0.66	371.33	bdl	360.26	bdl	bdl	44.19	bdl	bdl	bdl	bdl	10,601.25	bdl
14	bdl	bdl	21.69	bdl	bdl	bdl	bdl	0.43	bdl	bdl	bdl	bdl	bdl	bdl	bdl
15	bdl	bdl	48.03	bdl	bdl	bdl	bdl	0.15	bdl	bdl	bdl	bdl	bdl	bdl	bdl
16	bdl	bdl	5.04	bdl	bdl	bdl	bdl	bdl	bdl	bdl	bdl	bdl	bdl	bdl	bdl
17	bdl	bdl	102.52	bdl	bdl	bdl	bdl	bdl	bdl	bdl	bdl	bdl	bdl	bdl	bdl
18	bdl	670.26	144.22	756.61	bdl	bdl	bdl	bdl	bdl	bdl	bdl	bdl	bdl	bdl	bdl
19	bdl	1.02	0.40	22.43	105.93	83.24	bdl	bdl	54.94	bdl	0.76	bdl	bdl	bdl	bdl
20	15.83	11.32	3.71	36.49	20.44	7.82	1781.46	0.42	8.81	30.74	0.23	12.33	2.97	1248.30	1362.17
21	1430.24	1.84	3.40	79.63	6342.05	16.45	817.93	0.71	27.79	107.56	0.39	508.93	17.46	810.26	2603.88

5.7. Application of classifiers on Gunga deposit

Table 7 summarizes the classification results for pyrite data collected from the Gunga deposits. The four classifiers produced comparable results for the pyrite samples, with little difference observed between the two deposits, as most analyses focused on CD pyrite. In the MLP and GB models, 50 of the 60 data analyses were predicted to be CD pyrite, achieving an accuracy of >83.3 %.

The CD pyrite type was determined using the majority voting principle, as evidenced by the discrimination results. Only a limited amount of data, comprising a minimum of eight and a maximum of ten pyrite analyses, were predicted to be seawater pyrite. Furthermore, only a few data points were identified as magmatic-hydrothermal fluid pyrite, with a maximum of three using the MLP and SVM classifiers. This suggests that pyrite in the Gunga deposit is unlikely to be magmatic.

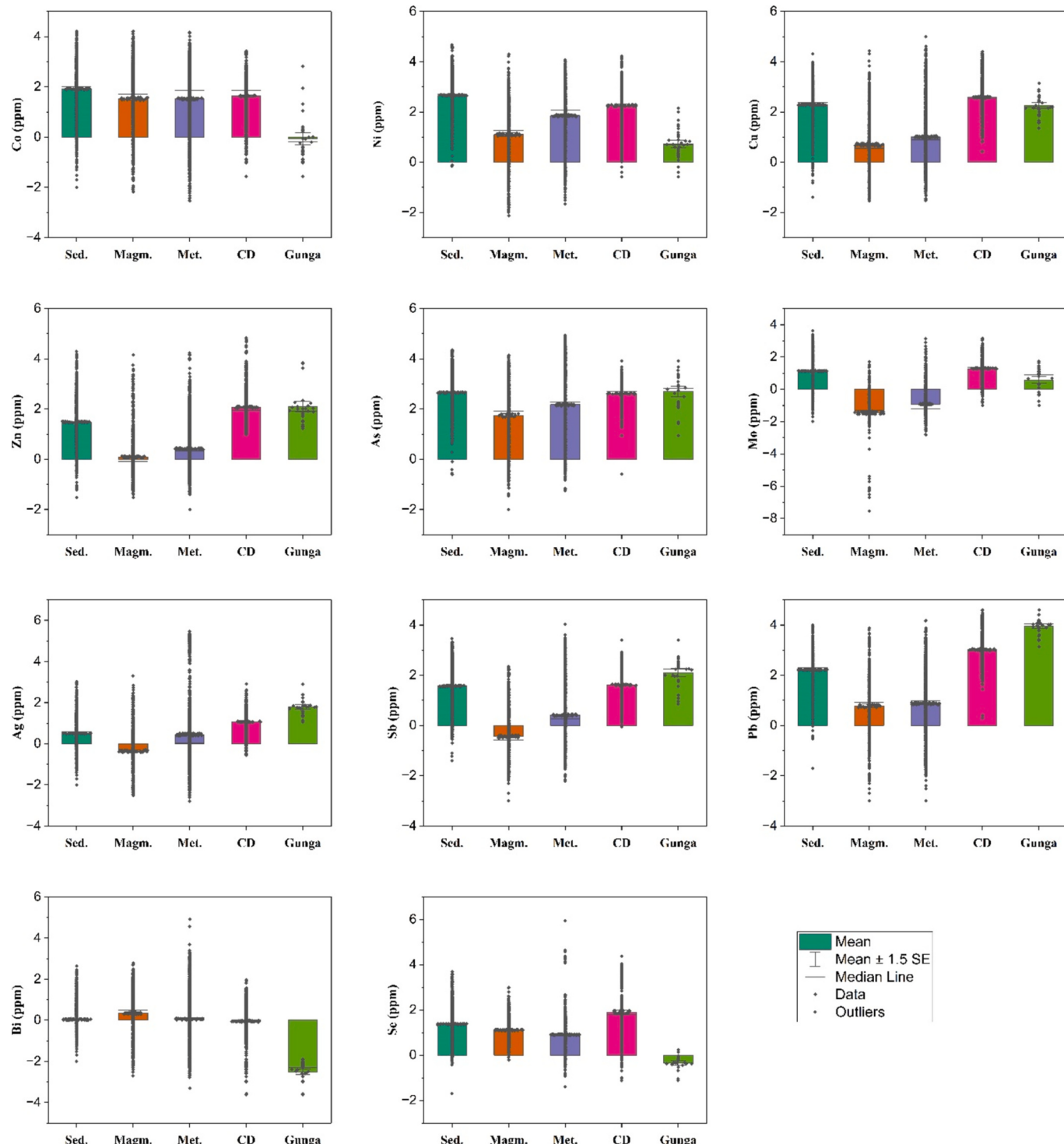


Fig. 9. Box plots of trace elements of Gunga Pb—Zn deposit and their comparison with global data for Pb—Zn deposits of different origin such as magmatic, metamorphic and CD. Sed.: Sedimentary, Met.: Magmatic, Metamorphic, CD: Clastic Dominant.

6. Discussion

6.1. Trace elements incorporation in pyrite

Previous research has shown that pyrite contains numerous trace elements. Thus, the trace element composition of pyrite can be utilized to analyze various geological settings and the evolution of hydrothermal fluids. Trace elements in pyrite can be found as mineral inclusions, such as visible micro-sized sulfide minerals, visible micro-sized oxide silicate

inclusions, invisible sulfide nanoparticles, and invisible solid solutions inside the crystal structure. Various elements, such As, Ag, Au, Co, Ni, Pb, Te and Se, can replace Fe and S in pyrite lattices (Deditius et al., 2008, 2014; Gregory, 2014; Keith et al., 2016; Martin et al., 2022).

Co and Ni exhibit the most significant association in the pyrite from the Gunga deposit, suggesting that Co and Ni may be integrated into the pyrite structure as $2\text{Fe}^{2+} \leftrightarrow \text{Co}^{2+} + \text{Ni}^{2+}$ (Fig. 13). Given that nearly all the samples exhibited Co/Ni ratios well below 1, it is more persuasive to suggest that Co^{2+} and Ni^{2+} directly replaced Fe^{2+} in pyrite, which is

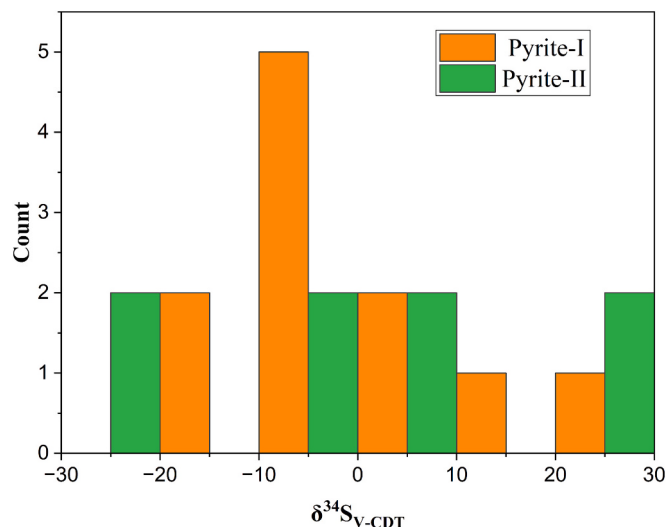


Fig. 10. S-isotope compositions in Pyrite-I and Pyrite-II from the Gunga Pb—Zn deposit.

Table 4
Sulfur isotope compositions in pyrite from Gunga deposit.

S no.	Mineral	$\delta^{34}\text{S}_{\text{V}-\text{CDT}}$
1	Pyrite-I	20.04
2		15.68
3		-1.56
4		-4.05
5		-14.22
6		6.24
7		-2.55
8		-1.12
9		1.38
10		-6.65
11		-15.05
12	Pyrite-II	-23.49
13		-22.78
14		26.22
15		25.86
16		-0.10
17		-1.89
18		0.81
19		1.45

Table 5
Pb isotope compositions in Pyrite from Gunga deposit.

S no.	$^{208}\text{Pb}/^{204}\text{Pb}$	$^{207}\text{Pb}/^{204}\text{Pb}$	$^{206}\text{Pb}/^{204}\text{Pb}$
1	38.77	15.70	18.56
2	38.77	15.70	18.56
3	38.76	15.70	18.55
4	38.77	15.70	18.56
5	38.76	15.70	18.55
6	38.76	15.70	18.55
7	38.76	15.70	18.55
8	38.77	15.70	18.56
9	38.75	15.70	18.56
10	38.76	15.70	18.56
11	38.77	15.70	18.56
12	38.72	15.69	18.55
13	38.75	15.70	18.56
14	38.75	15.70	18.56
15	38.71	15.69	18.55
16	38.73	15.69	18.55
17	38.62	15.66	18.51

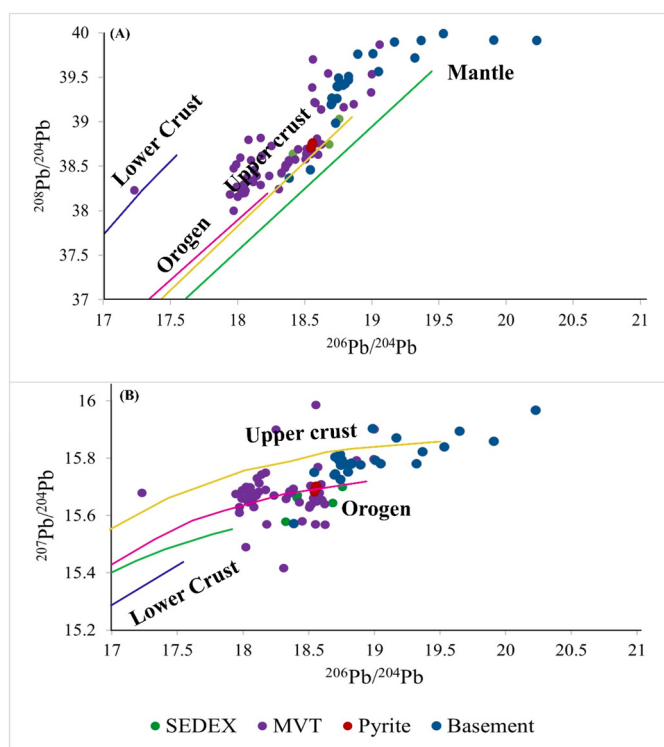


Fig. 11. Pb isotope compositions in pyrite from the Gunga Pb—Zn deposit and compared with sediment-hosted deposits in the Central Tethyan Domain and with Pb isotope composition of the Indian Plate (basement).

Table 6

Comparison of different ML model's performance in terms of Accuracy and AUC (mean values).

S. no.	ML model	Test accuracy	Validation accuracy	Test AUC	Validation AUC
1	RF	90.61	90.77	0.99	0.99
2	MLP	91.33	93.07	0.98	0.99
3	SVM	91.88	92.06	0.98	0.99
4	GB	91.88	91.60	0.99	0.99

consistent with previous research (H. Li et al., 2023; Xing et al., 2023; Yu et al., 2023). The significant relationship between Co and Ni can be explained by several parameters, such as temperature, sulfur fugacity, and the initial composition of the fluid. The substitution of Co and Ni was influenced by $f\text{S}_2$ and temperature. An increase in $f\text{S}_2$ and/or a decrease in temperature first promoted the equilibrium reaction $\text{Fe}^{2+} \leftrightarrow \text{Co}^{2+}$, followed by $\text{Fe}^{2+} \leftrightarrow \text{Ni}^{2+}$. The inclusion of As in pyrite has been extensively studied. It can be integrated into pyrite using three methods: replacing S^{2-} , replacing Fe^{2-} , and nanoinclusions of amorphous As-Fe-S trapped inside pyrite (Deditius et al., 2008, 2014). Within the Gunga deposit, there was a negative correlation between As and S, indicating that As had directly replaced S.

The ionic radius of Pb is significantly larger than that of Fe, making the direct substitution of Pb with Fe challenging. As in pyrite, Pb can disrupt pyrite lattices, enabling it to intrude into and replace Fe in these lattices. Higher concentrations allow elements with large ionic radii to be included in galena microinclusions (Chu et al., 2022; Ding et al., 2022; George et al., 2015; Hussain et al., 2021). The strong link between Zn and Fe suggests that Zn can directly substitute Fe. Monovalent and trivalent elements utilize a linked substitution mechanism for incorporation into the pyrite lattice.

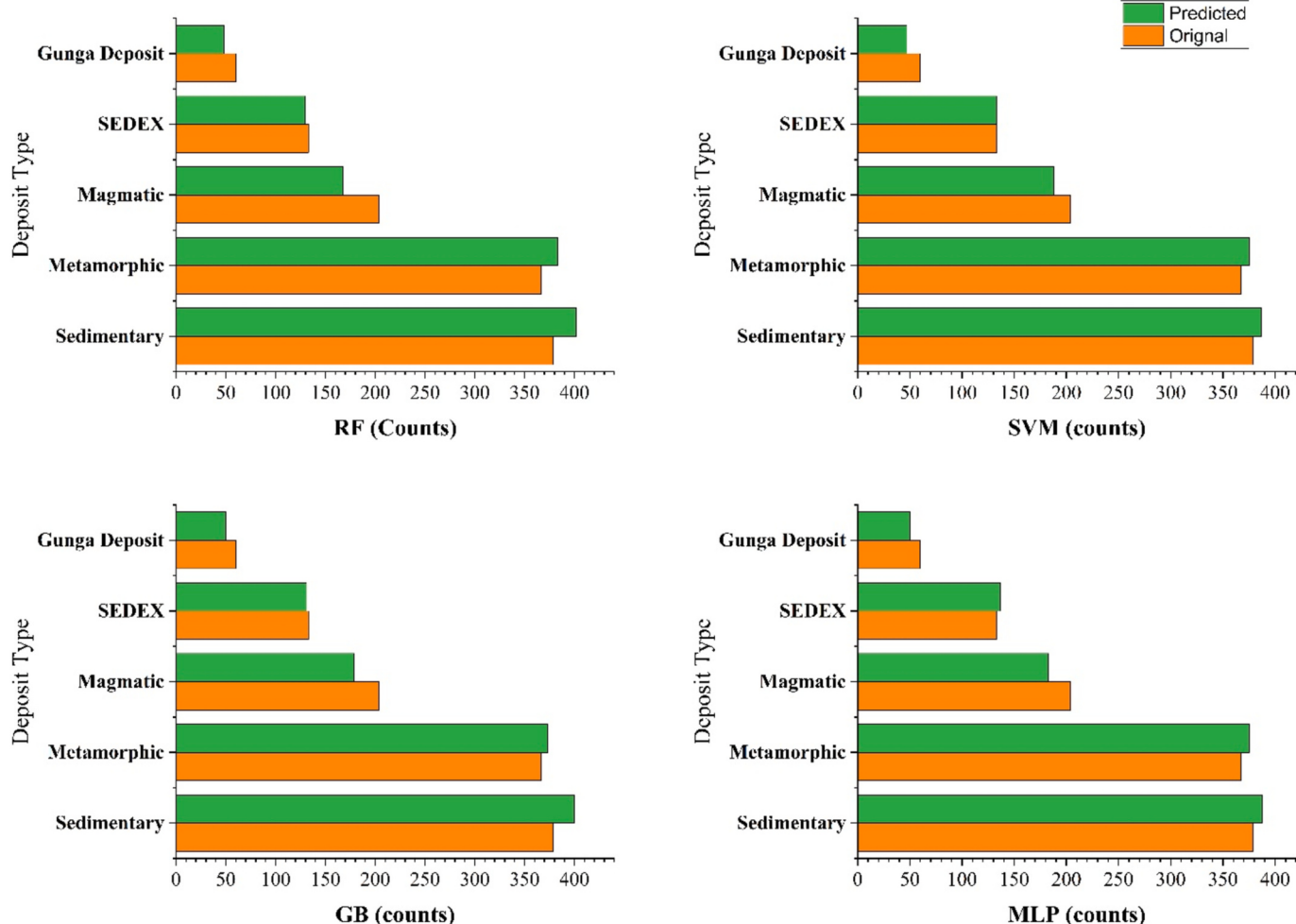


Fig. 12. Comparison of original and predicted deposit types based on the results of ML models.

Table 7
Metallogenetic discrimination results of four ML models on Gunga deposit.

S no.	Types	MLP	RF	SVM	GB
1	Magmatic	6	7	8	5
2	Metamorphic	1	1	2	1
3	SEDEX	50	48	47	50
4	Sedimentary	3	4	3	4

6.2. Source of sulfur and metals

Despite the different modes of $\delta^{34}\text{S}$ values for each pyrite type, the maximum $\delta^{34}\text{S}$ values are very similar and strongly negative, suggesting that the sulfur of the two types of pyrite in the Gunga deposit had the same source, namely seawater sulfate. To reliably estimate the $\delta^{34}\text{S}$ value of the source from the data for pyrite, it is necessary to know the temperature of pyrite deposition. Owing to the lack of fluid inclusions suitable for microthermometric analysis, we assume that the Gunga deposit formed at a temperature comparable to that of CD deposits elsewhere, i.e., 100 °C to 300 °C. At these temperatures, the sulfur isotope fractionation between pyrite and H₂S ($\epsilon^{34}\text{S}$ Pyrite-H₂S) was 2 ‰ and 1 ‰, respectively, and even at 10 °C, it was only 5 ‰. Based on this fractionation, the maximum $\delta^{34}\text{S}$ value analyzed for pyrite corresponds to a $\delta^{34}\text{S}$ value of H₂S in the mineralizing fluid of ~19 ‰ at 10 °C or 23 ‰ at 270 °C. Significantly, the $\delta^{34}\text{S}$ value of seawater for the Jurassic is estimated to have been 14–22 ‰. We therefore conclude that the sulfur for the Gunga deposit was sourced from coeval seawater sulfate, a

conclusion that has been drawn for most other stratiform sediment hosted Zn-Pb-(Ba) deposits (Bottrell and Newton, 2006; Seal, 2006).

6.2.1. Sulfate reduction pathways

Although seawater sulfate is ultimately the source of sulfur in the sulfide minerals of most CD deposits and sedimentary rocks, the sulfate reduction pathways may be different, as will the resulting sulfur isotope signatures. Bacterial sulfate reduction (BSR) will lead to very negative $\delta^{34}\text{S}$ values, as was the case for *syn-sedimentary* frambooidal pyrite in Howard's Pass CD Zn Pb deposit (~16.6 ‰ on average), whereas thermochemical sulfate reduction (TSR), which might occur during diagenesis, will produce very positive values. Sulfate reduction coupled with anaerobic oxidation of methane (SR-AOM), which occurs in the sulfate-methane transition zone (SMTZ) during diagenesis, would also produce H₂S with very positive $\delta^{34}\text{S}$ values (Bottrell and Newton, 2006; Seal, 2006). The reason for such different sulfur isotope signatures is that at the very low temperature of the BSR, the fractionation between sulfate and H₂S is very high, reaching 70 ‰ at the temperature of seawater on the ocean floor, whereas at the temperatures required for thermochemical sulfate reduction (TSR), it is very low, e.g., 15 ‰ at 150 °C (Seal, 2006). The positive $\delta^{34}\text{S}$ values of H₂S during SR-AOM were due to the rapid reduction of infiltrated sulfate in the sediment pores and the strong Rayleigh fractionation of sulfur isotopes during the oxidation of methane.

Studies conducted by Claypool et al. (1980) and Kampschulte and Strauss (2004) revealed long-term variations in seawater sulfate $\delta^{34}\text{S}$ values by examining the composition of sulfate minerals in marine

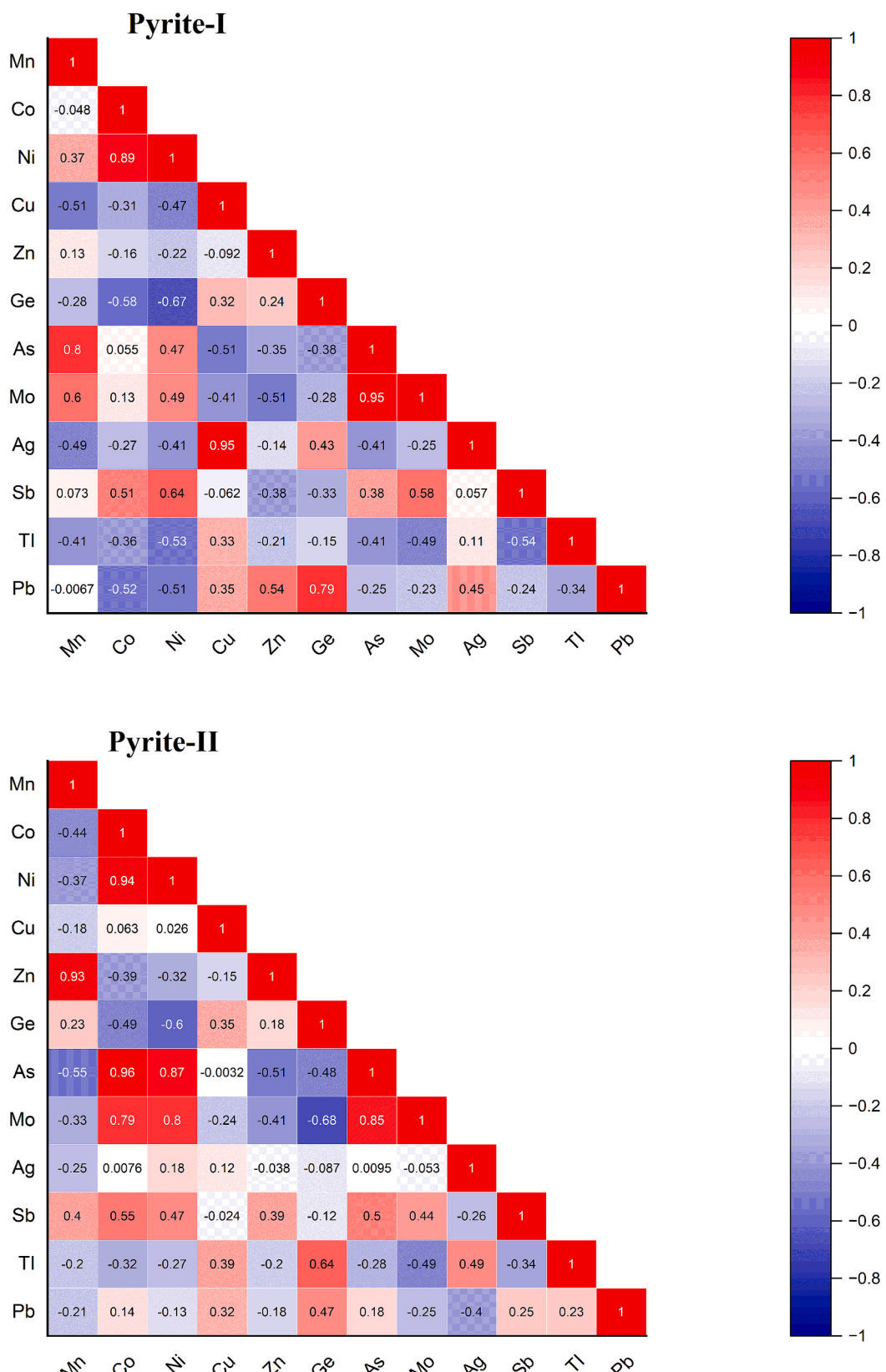


Fig. 13. Interelement correlations of molar ratios of minor and trace elements from Pyrite-I and Pyrite-II were based on the Pearson correlation coefficient.

evaporites. The sulfate values for Jurassic seawater ranged between $\delta^{34}\text{S}$ 14 to 22 ‰, as reported by Claypool et al. (1980) and Kampschulte and Strauss (2004), with a narrower range of 15 to 17 ‰, as stated by Bottrell and Newton (2006). Assuming the source of sulfur to be Jurassic seawater (14 to 22 ‰) and considering the minimum BSR fractionation (which varies between 20 and 70 ‰ with an average of 50 ‰), the minimum seawater sulfate $\delta^{34}\text{S}$ value would have been approximately -6 ‰. In the Gunga deposit, the majority of $\delta^{34}\text{S}$ values range from -24 to -0.16 ‰, which, when combined with low formation temperatures ($<150^\circ\text{C}$), suggests that BSR is the main sulfate reduction mechanism. Furthermore, the presence of frambooidal pyrite, high TOC values, and low-temperature elements in pyrite also supports this conclusion (Fig. 14).

6.2.2. Sources of Pb

Sulfide minerals typically have extremely low levels of U and Th, as well as minimal radiogenic Pb isotopes. This enabled the Pb isotopes present in sulfides from ore deposits to be employed to determine the source of Pb, regardless of the overall Pb concentration in the sulfides. The results showed that the Pb isotopes in pyrite from the study region had a constant chemical composition. The maximum analyzed samples were tightly clustered above the typical upper crustal Pb evolution line

in the Pb isotope Evolution Diagram created by Zartman and Doe (1981) (Fig. 11A), whereas in Fig. 11B, the maximum analyzed samples were clustered near the orogen curve. These results indicate diverse sources of Pb. These differences could be the result of several crustal sources that led to ore mineralization. Nonetheless, the ultimate source of Pb was crustal, similar to that of other Pb–Zn deposits in the Central Tethyan region. The high $^{206}\text{Pb}/^{204}\text{Pb}$ ratios during mineralization, as inferred from the computed μ values, also indicate the presence of crustal Pb sources (Zartman and Doe, 1981). The surrounding or underlying lithology of the deposits may be reflected in Pb isotope measurements. These findings suggest that the Pb–Zn mineralization in the Gunga deposit originated from crustal materials. The Pb isotope values of the Gunga deposit followed the same trend as those of the CD deposits worldwide (Hoggard et al., 2020; Leach et al., 2005).

The uniformity of the isotopic structure in ores depends on the degree of mixing and homogeneity of Pb before ore formation. The proposed explanations for this include Pb extraction from dense sedimentary layers or basement rocks, prolonged mechanical and/or chemical blending, and extensive lateral transportation over long distances, which could have resulted in the uniform distribution of Pb isotope ratios in large ore deposits. The consistent isotopic composition of the sulfides indicates that the Pb component in the Gunga deposit

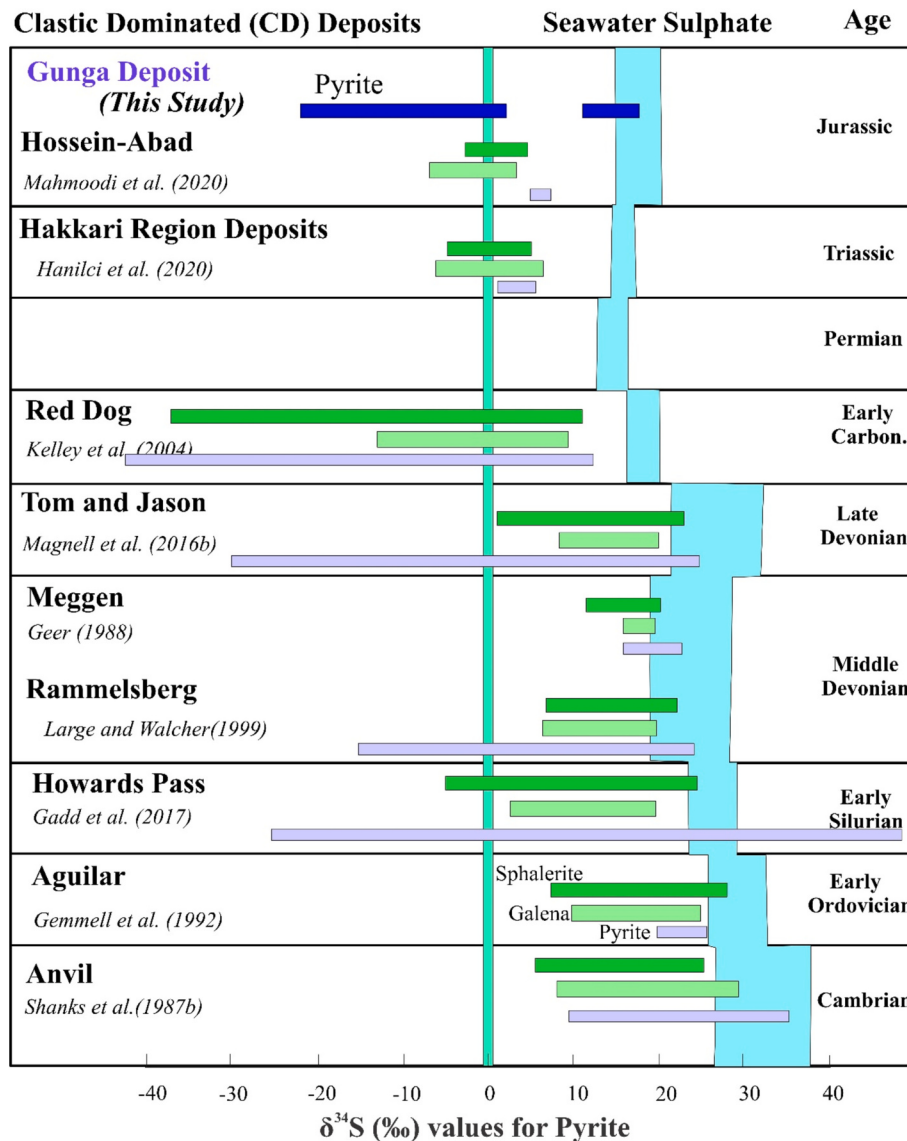


Fig. 14. S isotope compositions in Pyrite from Gunga Deposit compared with different Phanerozoic CD Pb–Zn deposits.

originated from a unified or well-mixed source.

6.3. Metallogenetic discrimination via machine learning (ML) algorithms

The classification of pyrite has been challenging because of its extensive chemical similarities to various forms. The trace elements found in the pyrite analyzed in this study closely matched the distribution range often observed in CD pyrite, including Cu, Zn, As, Ag, Sb, and Pb. However, these pyrite crystals exhibited similarities to magmatic pyrite, particularly in terms of Co, Ni, Se, and Bi (Fig. 9). In the conventional two-dimensional Co–Ni diagram, all classes of pyrite displayed significant differences and wide compositional similarities (Fig. 15). Overlaps were observed in the As–Co–Ni ternary diagram (Fig. 15), and the standard two-dimensional graphic was ineffective in distinguishing between the four forms of pyrites. The majority of the pyrite data in this study were located in overlapping regions of the four pyrite categories, leading to uncertain results. Comparing the pyrite results from the study region with the gathered data alone did not provide valuable insights (Qin et al., 2024; Zhong et al., 2021).

The pyrite data from the Gunga deposit were similar to those of the sedimentary and CD pyrite in the Co–Ni plot (Fig. 15). Nevertheless, the classification results are somewhat questionable. The trace element contents showed large variances; however, there was a significant compositional overlap across all forms of pyrite in the plot (Bhuyan and Hazarika, 2022; Qin et al., 2024; Sun and Zhou, 2022; Zhong et al., 2021). Thus, concentrating solely on discriminating a small number of components in a binary plot limits the capacity of pyrite composition to offer genetic importance. Multidimensional feature spaces have a greater discriminative capacity than binary or ternary feature spaces, enabling the successful classification of distinct groups.

The pyrite trace element data in high dimensions obtained by LA–ICP–MS successfully resolved the issue of unclear classification. The dataset was trained using four algorithms following data standardization, resulting in high classification accuracy, as shown in Table 6. The categorization outcomes of each method varied owing to changes in the basic assumptions, level of complexity, and variable settings. RF outperformed the other algorithms in classification, achieving the greatest efficiency on the dataset with an AUC of over 0.97 and an accuracy of over 89 %, as corroborated by Qin et al. (2024). The MLP and SVM algorithms capture intricate nonlinear relationships, filter out extraneous

data, and demonstrate robust generalization capabilities. MLP and RF algorithms are frequently used to solve classification problems (Qin et al., 2024; Zhong et al., 2021). The effectiveness of ML algorithms has been demonstrated in the genetic categorization of various minerals, such as pyrite, quartz, magnetite, and cassiterite.

The ML classification findings for pyrite data outperformed existing approaches, including the Co–Ni binary plot (accuracy =66.2 %) and quartz Al–Ti binary plot (accuracy =45 %) (Qin et al., 2024; Zhong et al., 2021). Using only a limited number of factors for classification may lead to subpar results, as shown in Fig. 15. Our classifiers achieved accuracy values comparable to those reported in previous studies that utilized supervised machine learning, ranging from 82 % to 98.9 % (Gregory et al., 2019; H. Li et al., 2023; Qin et al., 2024; Sun and Zhou, 2022; Yu et al., 2023). Typically, an accuracy rate of 90 % is considered strong for most classification problems, particularly when conventional methods are deemed inadequate. The results show that supervised machine learning is successful in predicting pyrite types.

6.3.1. Cross validations

In many cases, LA–ICP–MS data points are collected from the same specimen or a single pyrite grain. These data points are highly likely to be unintentionally divided into training and testing datasets. When this occurs, the classifier's performance on the testing set is overstated, because it is trained using highly similar data from the same specimen or pyrite grains.

This study evaluated the efficacy of machine learning-based classifiers using an approach called leave-one-group-out cross-validation. In this cross-validation method, the dataset was not equally and randomly partitioned. Rather, it comprised 134 subsets, with each subset containing all samples from a single deposit, and the classifiers were trained using samples from the remaining 133 deposits. By utilizing samples from an entirely new location, the performance of classifiers can be assessed, thereby avoiding the issue of encountering previously encountered data. This process of excluding the training and testing data was repeated 134 times for each deposit/stratum to gauge the effectiveness of the ML classifiers.

The deposit typically contained numerous pyrite samples, and the categorization outcome of the deposit/stratum was determined through a majority vote. For instance, if a deposit comprises 50 data points and the classifier, which has been trained, produces a result of 15 CD, 25

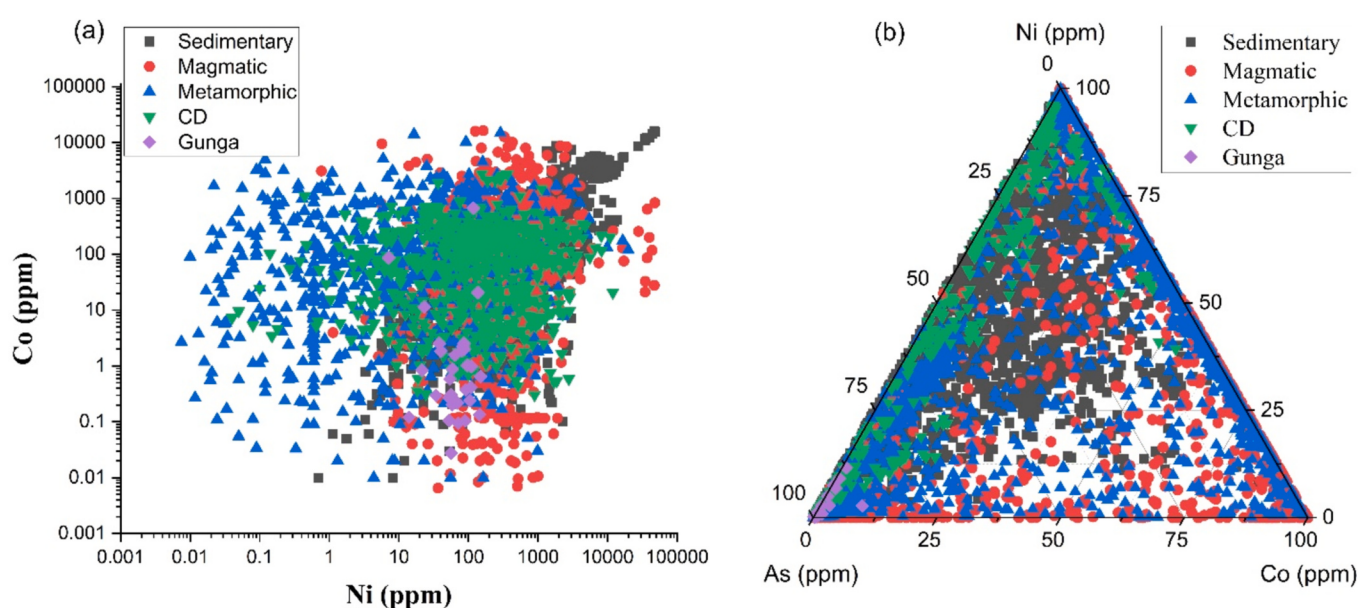


Fig. 15. (a) A biplot of Co vs. Ni from different Pb–Zn deposits for metallogenetic discrimination shows that different types of pyrite have compositional overlaps. (b) Ternary plot of As–Co–Ni from different Pb–Zn deposits for metallogenetic discrimination, which shows that different types of pyrite have compositional overlaps.

magmatic, and 10 metamorphic deposits, the categorization of this deposit is designated as VMS. Utilizing the ML-based classifiers, 121 of the 134 deposits/stratum were accurately identified through majority voting, resulting in an overall accuracy of >90 %. This suggests that ML-based classifiers are both robust and effective in distinguishing the origin of pyrite.

6.4. Implications for genesis in Gunga Pb—Zn deposit

6.4.1. Physicochemical conditions

6.4.1.1. Temperature. Certain elements present in pyrite, such As, Zn, Sb, and Pb, can serve as indicators of fluctuations in temperature throughout the mineralization process (Deditius et al., 2008, 2014; Figueroa and Gregory, 2017; Gregory et al., 2019; Mukherjee and Large, 2017; Qiu et al., 2018). The pyrite found in the Gunga deposit displayed elevated levels of these elements, suggesting that it formed under low-temperature conditions. The presence of a high concentration of As in pyrite is commonly indicative of a low-temperature environment in which it can replace sulfur and/or Fe within the pyrite structure. The average As levels in Pyrite-I (756 ppm) and Pyrite-II (2470 ppm) from the Gunga deposit suggest that the ore-forming fluids were at moderate to low temperatures.

The cobalt-to-nickel ratio of pyrite can be used as an indicator of the temperature. A Co/Ni ratio below 1 implies pyrite development at low temperatures, whereas a Co/Ni ratio above 1 predicts pyrite formation at high temperatures (H. Li et al., 2023; Xing et al., 2023). Pyrite-I had Co/Ni ratios below 1, whereas Pyrite-II had ratios over 1, suggesting that pyrite likely formed at low to moderate temperatures. Different levels of cobalt in pyrite indicate origins at high (>1000), moderate (100–1000), and low (<100) temperatures. The low Co percentages in Pyrite-I (average of 15 ppm) and Pyrite-II (average of 60 ppm) from the Gunga deposit suggest a low temperature for the fluids that formed the ore. Research has shown that pyrite typically develops at temperatures above 350 °C and contains high levels of Se, Co, Bi, and Ni. In contrast, pyrite found in the Gunga deposit had low concentrations of these elements, indicating a lower temperature formation (Fig. 8).

6.4.1.2. Redox conditions. Recent investigations have shown that the As(OH)₃ complex of As³⁺ is the primary As-containing species in natural hydrothermal systems across a broad spectrum of temperatures (25–500 °C) and fluid densities (0.05–1.1 g/cm³). Sb is susceptible to redox reactions, and its movement is greatly influenced by the redox environment. The major Sb species were Sb(OH)₅ and Sb(OH)₃ under oxidizing and reducing conditions, respectively. Sb(OH)₃ has a stronger binding affinity to Fe(hydr)oxides than Sb(OH)₅ across a broad pH range, often leading to the reduced mobility of Sb under reducing conditions. Under acidic and reducing conditions, both arsenic (As) and Sb form hydroxide complexes as As(OH)₃ and Sb(OH)₃, respectively. This results in As being more mobile than Sb, leading to high As/Sb ratios (Deditius et al., 2008, 2014; Ding et al., 2022; W.D. Zhang et al., 2022).

Pyrite-II in the Gunga deposit has a higher As/Sb ratio (average 31) compared to Pyrite-I (average 5.4), indicating that Pyrite-II is formed in a more acidic and reducing environment than Pyrite-I. Pyrite-I had a wide range of As/Sb ratios, indicating that the hydrothermal fluids responsible for its formation likely had more complex physicochemical conditions than those that formed Pyrite-II. Grejory proposed that As substitutes for S in reducing environments and Fe in oxidizing environments. In the Gunga deposit, As displays a negative correlation with S, indicating a decreasing trend.

6.4.2. Pyrite discrimination diagrams for CD Zn—Pb

A fertility diagram was created using pyrite data from the Gunga deposit, focusing on Ni, Mo, Zn, As, and Tl. Black shale sedimentary pyrite is not associated with CD mineralization and serves as a source of

marine pyrite in unproductive black shales. The x-axis in this image represents the combination of two elements, Ni and 2Mo, which are taken up by pyrite from seawater and are not connected to hydrothermal processes. The y-axis equation 2Zn + 5As + 20Tl represents three elements primarily derived from CD hydrothermal activity (Fig. 16). The multipliers in both statements were intended to provide equal weights for each TE (Cameron, 2011; Mukherjee and Large, 2017; Magnall et al., 2021).

Most assessments of the Gunga deposit indicate a tendency toward hydrothermal elements, as shown in Fig. 16. Mo, Ni, Co, Se, and As were adsorbed onto pyrite from the water column and reflected the current trace element concentrations in the seawater. Riverine flow is the main source of these elements in the oceans. The oxidative weathering of land is thought to transport elements in soluble forms (such as MoO₄²⁻, Ni²⁺, SeO₃²⁻, and SeO₄²⁻) to the ocean through riverine flow. These elements then become part of pyrite when they reach the redox boundary at or below the sediment-water interface. Elements such as Zn, Tl, Cu, Pb, Ag, and As found in seawater were mostly introduced into the water column through hydrothermal exhalations associated with CD mineralization.

6.4.3. Ore genesis

Identifying the source of hydrothermal fluids is crucial for understanding the formation of Pb—Zn deposits (Gregory et al., 2019; Leach et al., 2005). According to data-driven machine learning predictions, the ore-forming fluid in the Gunga deposit is primarily CD hydrothermal fluid, which aligns with other geological and geochemical findings. The in-situ δ³⁴S measurements of pyrite from the Gunga deposit range from -22 to +22 ‰, indicating that sulfur primarily originated from seawater rather than magma, unlike other magmatic and metamorphic deposits (0 to 5 ‰). Most CD deposits are believed to include metals originating from the Earth's crust, as shown by Pb isotope compositions (Leach et al., 2005, 2010). The isotopic compositions of the Gunga deposit suggest that the economic metals in the deposit originated primarily from the Earth's crust.

The majority of low-temperature Pb—Zn deposits in the Lasbela-Khuzdar metallogenetic region are primarily found in Jurassic rock layers that have experienced significant hydrothermal mineralization during Indian Plate rifting events, as reported by S.Nayar Ahsan (1997) and confirmed by studies conducted by Song et al. (2019, 2023) and Ahsan and Mallick (1999). The Gunga deposit, situated in the passive-edge tectonic setting of the Indian Plate, is similar to other deposits in

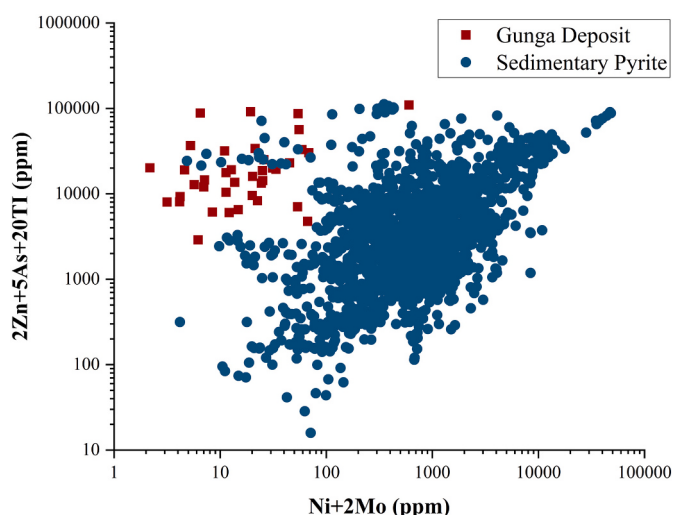


Fig. 16. Fertility diagram of pyrite from the Gunga deposit and barren sedimentary pyrite from published literature to discriminate CD pyrite from barren sedimentary pyrite.

the vicinity, and its features align with those of the global CD deposits. Consequently, the Gunga deposit was classified as CD deposit.

The application of machine learning to big data analysis of pyrite geochemistry provides robust evidence for determining the types of ore-forming fluids, facilitating the distinction between ore genesis, particularly in controversial ore deposits. The efficiency and cost-effectiveness of this approach make it promising for key metal discovery in the early stages. Supervised machine learning classification algorithms have the potential for a range of classification tasks in economic geology, including mineral or ore deposit classification, provided that sufficient training data are available, as demonstrated in recent studies by H. Li et al. (2023), Qin et al. (2024), and Sun et al. (2022).

7. Conclusions

This study highlights the successful application of ML algorithms in classifying pyrite types and improving understanding of Pb–Zn deposit genesis. Using LA-ICP-MS trace element data from over 5400 data points from different Pb–Zn deposits, this study overcame limitations of traditional two-dimensional plots showing significant overlaps. Among algorithms used, RF achieved the highest classification accuracy with an AUC over 0.97 and accuracy above 90 %, outperforming traditional methods like Co–Ni binary plots (66.2 % accuracy). Cross-validation using leave-one-group-out (LOGO) on 134 subsets ensured robust classifier performance, validating models against unseen data. Key elements for classification included As, Sb, Zn, Pb, Ag, and Tl, reflecting hydrothermal processes, while Co and Ni indicated depositional temperatures.

The research also presented the first detailed geochemical analysis of the Gunga Pb–Zn deposit in the Lasbela-Khuzdar region, classifying it as a Clastic-Dominant (CD)-type deposit. Sulfur isotope data indicated BSR with seawater sulfate as the primary sulfur source, while lead isotopes confirmed a crustal origin for the metals. The deposit formed under low to moderate temperatures (~100–300 °C), with variations in redox conditions and sulfur fugacity influencing trace element incorporation. High As/Sb ratios in pyrite-II suggested formation under acidic and reducing conditions, while pyrite-I reflected more variable physicochemical conditions.

This study emphasizes ML's growing potential in mineral exploration by efficiently handling complex datasets and improving outcomes, especially in areas with limited surface geological information. These findings underscore ML algorithms' importance in guiding new deposit discovery and refining mineralized system classification, making them promising for economic geological applications.

Supplementary data to this article can be found online at <https://doi.org/10.1016/j.gexplo.2025.107693>.

CRediT authorship contribution statement

Muhammad Amar Gul: Writing – review & editing, Writing – original draft, Software, Methodology, Investigation, Formal analysis, Data curation, Conceptualization. **Huishan Zhang:** Writing – review & editing, Supervision, Resources, Project administration, Investigation, Formal analysis. **Yanguang Li:** Writing – review & editing, Resources, Project administration, Investigation, Formal analysis. **Xiaoyong Yang:** Writing – review & editing, Validation, Supervision, Resources, Project administration, Funding acquisition, Conceptualization. **Chao Sun:** Writing – review & editing, Validation, Resources, Investigation. **Xiaojian Zhao:** Validation, Resources, Funding acquisition. **Guangli Ren:** Validation, Resources, Project administration, Funding acquisition, Data curation. **Asia Kanwal:** Visualization, Software, Methodology, Investigation, Formal analysis, Data curation, Conceptualization. **Muhammad Hafeez:** Writing – review & editing, Visualization, Investigation, Data curation. **Yu Yang:** Writing – review & editing, Visualization, Data curation. **Rizwan Sarwar Awan:** Writing – review & editing, Visualization, Validation. **Mohamed Faisal:** Writing – review & editing, Visualization, Validation, Supervision, Investigation.

Consent to publish

Not applicable.

Ethical approval

This manuscript has not been published elsewhere in part or in entirety and is not under consideration by another journal. We have read and understood your journal's policies, and we believe that neither the manuscript nor the study violates any of these. We have not submitted our manuscript to a preprint server before submitting it to the Journal of Geochemical Exploration.

Consent to participate.

Not applicable.

Declaration of competing interest

The authors declare the following financial interests/personal relationships which may be considered as potential competing interests: The research is financially supported by the National Natural Science Foundation of China (42372115, 92055314), the Innovation Capability Support Program of Shaanxi Province (2022KJXX-91), International Geoscience Program (IGCP-741), and China Geological Survey program (DD20201159).

Acknowledgments

The research is financially supported by the National Natural Science Foundation of China (42372115, 92055314), the Innovation Capability Support Program of Shaanxi Province (2022KJXX-91), International Geoscience Program (IGCP-741), and China Geological Survey program (DD20201159). We are thankful to Bolan Mining Comapny (BME) Pakistan for their help during field visit.

Data availability

Data will be made available on request.

References

- Ahsan, S.N., Mallick, K.A., 1999. Geology and genesis of barite deposits of Lasbela and Khuzdar districts, Balochistan, Pakistan. *Resour. Geol.* <https://doi.org/10.1111/j.1751-3928.1999.tb00036.x>.
- Alferez, G.H., Esteban, O.A., Clausen, B.L., Ardiña, A.M.M., 2022. Automated machine learning pipeline for geochemical analysis. *Earth Sci. Inf.* 15 (3), 1683–1698. <https://doi.org/10.1007/s12145-022-00821-8>.
- Bhuyan, N., Hazarika, P., 2022. Ore genetic implications of pyrite and sphalerite compositions from Rajputa-Dariba and Zawarmala Pb-Zn deposits, Northwestern India. *Geol. J.* 57 (11), 4634–4661. <https://doi.org/10.1002/gj.4562>.
- Bottrell, S.H., Newton, R.J., 2006. Reconstruction of changes in global sulfur cycling from marine sulfate isotopes. *Earth Sci. Rev.* 75 (1–4), 59–83. <https://doi.org/10.1016/j.earscirev.2005.10.004>.
- Cameron, R., 2011. Title Pyrite Trace Element Haloes to Northern Australian SEDEX Deposits. <https://doi.org/10.25959/23228402.v1>.
- Chu, X., Li, B., Shen, P., Zha, Z., Lei, Z., Wang, X., Tao, S., Hu, Q., 2022. Trace elements in sulfide minerals from the Huangshaping copper-polymetallic deposit, Hunan, China: ore genesis and element occurrence. *Ore Geol. Rev.* 144. <https://doi.org/10.1016/j.oregeorev.2022.104867>.
- Claypool, G.E., Holser, W.T., Kaplan, I.R., Sakai, H., Zák, I., 1980. The age curves of sulfur and oxygen isotopes in marine sulfate and their mutual interpretation 1. *Chem. Geol.* 28.
- Cui, H., Deng, Y., Zhong, R., Li, W., Yu, C., Danyushevsky, L.V., Belousov, I., Li, Z., Wang, H., 2023. Determining the ore-forming processes of Dongshengmiao Zn-Pb-Cu deposit: evidence from the linear discriminant analysis of pyrite geochemistry. *Ore Geol. Rev.* 163. <https://doi.org/10.1016/j.oregeorev.2023.105782>.
- Deditius, A.P., Utsunomiya, S., Renock, D., Ewing, R.C., Ramana, C.V., Becker, U., Kesler, S.E., 2008. A proposed new type of arsenian pyrite: composition, nanostructure and geological significance. *Geochim. Cosmochim. Acta* 72 (12), 2919–2933. <https://doi.org/10.1016/j.gca.2008.03.014>.
- Deditius, A.P., Reich, M., Kesler, S.E., Utsunomiya, S., Chryssoulis, S.L., Walshe, J., Ewing, R.C., 2014. The coupled geochemistry of Au and As in pyrite from hydrothermal ore deposits. *Geochim. Cosmochim. Acta* 140, 644–670. <https://doi.org/10.1016/j.gca.2014.05.045>.

- Ding, T., Tan, T., Wang, J., Ma, D., Lu, J., Zhang, R., Liang, J., 2022. Trace-element composition of pyrite in the Baoshan Cu-Mo-Pb-Zn deposit, southern Hunan Province, China: insights into the ore genesis. *Ore Geol. Rev.* 147. <https://doi.org/10.1016/j.oregeorev.2022.104989>.
- Dmitrijeva, M., Cook, N.J., Ehrig, K., Ciobanu, C.L., Metcalfe, A.V., Kamenetsky, M., Kamenetsky, V.S., Gilbert, S., 2020. Multivariate statistical analysis of trace elements in pyrite: prediction, bias and artefacts in defining mineral signatures. *Minerals* 10 (1). <https://doi.org/10.3390/min10010061>.
- Figueroa, M.C., Gregory, D.D., 2017. Isotopic and elemental chemistry of sedimentary pyrite: a combined analytical and statistical approach to a novel planetary biosignature. <https://www.researchgate.net/publication/323585344>.
- Frenzel, M., Voudouris, P., Cook, N.J., Ciobanu, C.L., Gilbert, S., Wade, B.P., 2022. Evolution of a hydrothermal ore-forming system recorded by sulfide mineral chemistry: a case study from the Plaka Pb-Zn-Ag Deposit, Lavrion, Greece. *Mineral. Deposita* 57 (3), 417–438. <https://doi.org/10.1007/s00126-021-01067-y>.
- George, L., Cook, N.J., Ciobanu, C.L., Wade, B.P., 2015. Trace and minor elements in galena: A reconnaissance LA-ICP-MS study. *Am. Mineral.* 100 (2–3), 548–569. <https://doi.org/10.2138/am-2015-4862>.
- Gregory, D.D., 2014. The Trace Element Composition of Sedimentary Pyrite: Factors Effecting Uptake and Uses of the Data for Determining Paleo-ocean Conditions.
- Gregory, D.D., Cracknell, M.J., Large, R.R., McGoldrick, P., Kuhn, S., Maslennikov, V.V., Baker, M.J., Fox, N., Belousov, I., Figueroa, M.C., Steadman, J.A., Fabris, A.J., Lyons, T.W., 2019. Distinguishing ore deposit type and barren sedimentary pyrite using laser ablation-inductively coupled plasma-mass spectrometry trace element data and statistical analysis of large data sets. *Econ. Geol.* 114 (4), 771–786. <https://doi.org/10.5382/econgeo.4654>.
- Gul, M.A., Yang, X., Zhang, H., Akhtar, S., Faisal, M., 2020. Sediment-hosted Pb-Zn deposits in Pakistan. 36th International Geological Congress, New Delhi, India.
- Han, S., Li, M., Ren, Q., 2019. Discriminating among tectonic settings of spinel based on multiple machine learning algorithms. *Big Earth Data* 3 (1), 67–82. <https://doi.org/10.1080/20964471.2019.1586074>.
- Hasterok, D., Halpin, J.A., Collins, A.S., Hand, M., Kreemer, C., Gard, M.G., Glorie, S., 2022. New maps of global geological provinces and tectonic plates. *Earth Sci. Rev.* 231, 104069. <https://doi.org/10.1016/j.earscirev.2022.104069>.
- He, Y., Zhou, Y., Wen, T., Zhang, S., Huang, F., Zou, X., Ma, X., Zhu, Y., 2022. A review of machine learning in geochemistry and cosmochemistry: method improvements and applications. In: *Applied Geochemistry*, vol. 140. Elsevier Ltd. <https://doi.org/10.1016/j.apgeochem.2022.105273>
- Hoggard, M.J., Czarnota, K., Richards, F.D., Huston, D.L., Jaques, A.L., Ghelichkhan, S., 2020. Global distribution of sediment-hosted metals controlled by craton edge stability. *Nat. Geosci.* 13 (7), 504–510. <https://doi.org/10.1038/s41561-020-0593-2>.
- Husain, V., Khan, H., Germann, K., & Zak, K. (2002). Geochemical investigations of stratabound Gunga barite deposits of Khuzdar (Balochistan), Pakistan. *Resource Geology*. doi:<https://doi.org/10.1111/j.1751-3928.2002.tb00116.x>.
- Hussain, Z., Tao, C., Li, C.F., Liao, S., Alam, M., Farhan, M., Zhang, H., Hussain, A., 2021. Mineralogy, fluid inclusions, and isotopic study of the kargah cu-pb polymetallic vein-type deposit, kohistan island arc, northern Pakistan: implication for ore genesis. *Minerals* 11 (11). <https://doi.org/10.3390/min11111266>.
- Jancovic, S., 1986. The Mineral Assiation and Genesis of Lead Zinc Barite Deposits of Gunga Khuzdar Balochistan. *Geological Survey of Pakistan*.
- Kampschulte, A., Strauss, H., 2004. The sulfur isotopic evolution of Phanerozoic seawater based on the analysis of structurally substituted sulfate in carbonates. *Chem. Geol.* 204 (3–4), 255–286. <https://doi.org/10.1016/j.chemgeo.2003.11.013>.
- Keith, M., Häckel, F., Haase, K.M., Schwarz-Schampera, U., Klemd, R., 2016. Trace element systematics of pyrite from submarine hydrothermal vents. *Ore Geol. Rev.* 72, 728–745. <https://doi.org/10.1016/j.oregeorev.2015.07.012>.
- Leach, D.L., Sangster, D.F., Kelley, K.D., Large, R.R., Garven, G., Allen, C.R., Gutzmer, J., Walters, S., 2005. Sediment-hosted lead-zinc deposits: a global perspective. *Econ. Geol.*
- Leach, D.L., Bradley, D.C., Huston, D., Pisarevsky, S.A., Taylor, R.D., Gardoll, S.J., 2010. Sediment-hosted lead-zinc deposits in earth history. *Econ. Geol.* <https://doi.org/10.2113/gsgecongeo.105.3.593>.
- Li, X.M., Zhang, Y.X., Li, Z.K., Zhao, X.F., Zuo, R.G., Xiao, F., Zheng, Y., 2023a. Discrimination of Pb-Zn deposit types using sphalerite geochemistry: new insights from machine learning algorithm. *Geosci. Front.* 14 (4). <https://doi.org/10.1016/j.gsf.2023.101580>.
- Li, H., Zhu, D.P., Algeo, T.J., Li, M., Jiang, W.C., Chen, S.F., Elatikpo, S.M., 2023b. Pyrite trace element and S-Pb isotopic evidence for contrasting sources of metals and ligands during superimposed hydrothermal events in the Dongping gold deposit, North China. *Mineral. Deposita* 58 (2), 337–358. <https://doi.org/10.1007/s00126-022-01128-w>.
- Magnall, J.M., Hayward, N., Gleeson, S.A., Schleicher, A., Dalrymple, I., King, R., Mahlstadt, N., 2021. The Teena Zn-Pb Deposit (McArthur Basin, Australia). Part II:
- carbonate replacement sulfide mineralization during burial diagenesis- implications for mineral exploration. *Econ. Geol.* 116 (8), 1769–1801. <https://doi.org/10.5382/econgeo.4845>.
- Martin, A.J., McDonald, I., Jamieson, J.W., Jenkin, G.R.T., McFall, K.A., Piercy, G., MacLeod, C.J., Layne, G.D., 2022. Mineral-scale variation in the trace metal and sulfur isotope composition of pyrite: implications for metal and sulfur sources in mafic VMS deposits. *Mineral. Deposita* 57 (6), 911–933. <https://doi.org/10.1007/s00126-021-01080-1>.
- Mukherjee, I., Large, R., 2017. Application of pyrite trace element chemistry to exploration for SEDEX style Zn-Pb deposits: McArthur Basin, Northern Territory, Australia. *Ore Geol. Rev.* 81, 1249–1270. <https://doi.org/10.1016/j.oregeorev.2016.08.004>.
- Mukherjee, I., Large, R.R., Bull, S., Gregory, D.G., Stepanov, A.S., Ávila, J., Ireland, T.R., Corkrey, R., 2019. Pyrite trace-element and sulfur isotope geochemistry of paleomesoproterozoic McArthur Basin: proxy for oxidative weathering. *Am. Mineral.* 104 (9), 1256–1272. <https://doi.org/10.2138/am-2019-6873>.
- Qin, Y., Kong, H., Liu, B., Jiang, H., Hou, X., Huang, J., 2024. Distinguishing the type of ore-forming fluids in gold deposits using pyrite geochemistry and machine learning. *Nat. Resour. Res.* 33 (1), 107–127. <https://doi.org/10.1007/s11053-023-10282-5>.
- Qiu, W.J., Zhou, M.F., Li, X., Williams-Jones, A.E., Yuan, H., 2018. The genesis of the giant Dajiangping SEDEX-type pyrite deposit, South China. *Econ. Geol.* 113 (6), 1419–1446. <https://doi.org/10.5382/econgeo.2018.4597>.
- S.Nayar Ahsan, I.H.Q., 1997. Mineral resources of Lasbela and Khuzdar Districts, Balochistan, Pakistan. *Geology Bul. Uni. Peshawar* 30, 41–51.
- Seal, R.R., 2006. Sulfur isotope geochemistry of sulfide minerals. *In. Rev. Mineral. Geochim.* 61, 633–677. <https://doi.org/10.2138/rmg.2006.61.12>.
- Song, Y., Liu, Y., Hou, Z., Fard, M., Zhang, H., Zhuang, L., 2019. Sediment-hosted Pb-Zn deposits in the Tethyan domain from China to Iran: Characteristics, tectonic setting, and ore controls. *Gondwana Res.* 75, 249–281. <https://doi.org/10.1016/j.gr.2019.05.005>.
- Song, Y., Hou, Z., Liu, Y., Zhuang, L., Hu, G., 2023. Mississippi Valley-type Zn-Pb deposits in orogenic thrust belts: ore formation in response to synorogenic crustal transgression or extension. *Mineral. Deposita*. <https://doi.org/10.1007/s00126-023-01185-9>.
- Sun, G.T., Zhou, J.X., 2022. Application of machine learning algorithms to classification of Pb-Zn deposit types using LA-ICP-MS data of sphalerite. *Minerals* 12 (10). <https://doi.org/10.3390/min12101293>.
- Sun, G., Zeng, Q., Zhou, J.X., 2022. Machine learning coupled with mineral geochemistry reveals the origin of ore deposits. *Ore Geol. Rev.* 142. <https://doi.org/10.1016/j.oregeorev.2022.104753>.
- Williams, M., Klump, J., Barnes, S., 2019. Multivariate geochemical tectonic discrimination: practical approaches, limitations and opportunities. *Explor. Geophys.* 2019 (1). <https://doi.org/10.1080/22020586.2019.12073190>.
- Xing, L., Li, W., Zang, M., Yang, F., Liu, J., Shi, Y., Guo, L., Li, P., 2023. Genesis and mineralization implications of dissolution-regrowth pyrite in the large Qukulekedong Au-Sb deposit, East Kunlun, NW China. *Ore Geol. Rev.* 157. <https://doi.org/10.1016/j.oregeorev.2023.105448>.
- Yu, Q., Wang, Z., Sun, Q., Wang, K., 2023. In situ trace element and sulfur isotope composition of pyrite from the Beiwagou Pb-Zn deposit, Liaodong Peninsula, Northeast China: implications for ore genesis. *Minerals* 13 (9). <https://doi.org/10.3390/min13091176>.
- Zaigham, N.A., Mallick, K.A., 2000. Bela ophiolite zone of southern Pakistan: tectonic setting and associated mineral deposits. *Bull. Geol. Soc. Am.* [https://doi.org/10.1130/0016-7606\(2000\)112<478:BOZOSP>2.0.CO;2](https://doi.org/10.1130/0016-7606(2000)112<478:BOZOSP>2.0.CO;2).
- Zartman, R.E., Doe, B.R., 1981. *Plumbotectonics-The Model*, Vol. 75.
- Zhang, W.D., Li, B., Lu, A.H., Zhao, K.D., Elatikpo, S.M., Chen, X.D., Zhu, L., Yu, M., 2022a. In-situ pyrite trace element and sulfur isotope characteristics and metallogenetic implications of the Qixiashan Pb-Zn-Ag polymetallic deposit, Eastern China. *Ore Geol. Rev.* 144. <https://doi.org/10.1016/j.oregeorev.2022.104849>.
- Zhang, J., Shao, Y., Liu, Z., Chen, K., 2022b. Sphalerite as a record of metallogenetic information using multivariate statistical analysis: constraints from trace element geochemistry. *J. Geochem. Explor.* 232. <https://doi.org/10.1016/j.jgx.2021.106883>.
- Zhang, Huishan, Song, Yucai, Sun, Jianing, Jun, Hong, Yasir Shaheen, Khalil, Li, Yanguang, Zhang, Haidi, Wang, Zhihua, 2024. A new discovery of mineralization as subseafloor hydrothermal replacement in the dudar super-large SEDEX lead-zinc deposit in Pakistan. *J. Earth Sci.* 35 (3), 1075–1078. <https://doi.org/10.1007/s12583-024-2015-7>.
- Zhong, R., Deng, Y., Li, W., Danyushevsky, L.V., Cracknell, M.J., Belousov, I., Chen, Y., Li, L., 2021. Revealing the multi-stage ore-forming history of a mineral deposit using pyrite geochemistry and machine learning-based data interpretation. *Ore Geol. Rev.* 133. <https://doi.org/10.1016/j.oregeorev.2021.104079>.